UNIVERSITY OF CALIFORNIA, SAN DIEGO

Low Velocity Blunt Impact on Lightweight Composite Sandwich Panels

A Thesis submitted in partial satisfaction of the requirements
for the degree Master of Science

in

Structural Engineering

by

Monica Kar Chan

Committee in charge:

Professor Hyonny Kim, Chair
Professor Chiara Bisagni
Professor Francesco Lanza di Scalea

2014

The Thesis of Monica Kar Chan is approved and it is acceptable in quality and form for publication on microfilm and electronically:

_____

_____

_____
Chair

University of California, San Diego

2014

TABLE OF CONTENTS

LIST OF FIGURES

LIST OF TABLES

ACKNOWLEDGEMENTS

I would like to thank Professor Hyonny Kim for giving me the opportunity to work on this research project and contribute to the future of this field. I am very appreciative of his guidance and support, which has made this thesis and research possible. He has helped me develop my skills and discover the passion and inspiration to succeed in endeavors beyond just aerospace structures and research.

I would like to thank all my professors I have had in both my undergraduate and graduate careers at UC San Diego for sharing their diverse knowledge and perspectives. I would also like to thank the other students in lab for their assistance, especially in learning how to operate lab equipment.

I would also like to thank my parents, my sister, my brother, and my friends for their continuous support and encouragement in all my endeavors. They have helped me get to where I am today, and I am forever grateful.

Thank you.

ABSTRACT OF THE THESIS

Low Velocity Blunt Impact on Lightweight Composite Sandwich Panels

by

Monica Kar Chan

Master of Science in Structural Engineering

University of California, San Diego, 2014

Professor Hyonny Kim, Chair

There is an increased desire to incorporate more composite sandwich structures into modern aircrafts. Because in-service aircrafts routinely experience impact damage during maintenance due to ground vehicle collision, dropped equipment, or foreign object damage (FOD) impact, it is necessary to understand their impact characteristics,

particularly when blunt impact sources create internal damage with little or no external visibility.

The objective of this investigation is to explore damage formation in lightweight composite sandwich panels due to low-velocity impacts of variable tip radius and energy level. The correlation between barely visible external dent formation and internal core damage was explored as a function of impact tip radius. A pendulum impactor was used to impact composite sandwich panels having honeycomb core while held in a 165 mm square window fixture. The panels were impacted by hardened steel tips with radii of 12.7, 25.4, 50.8, and 76.2 mm at energy levels ranging from 2 to 14 J.

Experimental data showed little dependence of external dent depth on tip radius at very low energies of 2 to 6 J, and thus, there was also little variation in visibility due to tip radius. Four modes of internal core damage were identified. Internal damage span and depth were dependent on impact tip radius. Damage depth was also radius-dependent, but stabilized at constant depth independent of kinetic energy. Internal damage span increased with increasing impact energy, but not with increasing tip radius, suggesting a relationship between maximum damage tip radius with core density/size.

1 INTRODUCTION

1.1 MOTIVATION

Advanced composites are becoming widely used in the aerospace industry, with an increased desire to incorporate more composite sandwich structures. Composite sandwich structures have high strength and stiffness to weight ratios as well as high corrosion resistance, making it an efficient way to increase stiffness without a large increase in structural weight. However, their impact characteristics are not well understood , particularly when blunt impact sources create internal damage with little or no external visibility.

In-service aircraft routinely experience impact damage during maintenance due to collisions with ground vehicles, dropped equipment, or foreign object damage (FOD) impact, and can result in complex behavior in the core. The sandwich structure may exhibit damage modes such as fiber failure, matrix cracking, delamination, core crushing and shear, core wall buckling (or kinking) and fracture [1]. These types of damage may propagate quickly throughout the core due to fatigue loading during repetitive ground-air-ground cycles and can significantly reduce structural performance [2]. Visual inspection of external damage is not always a clear indicator of the extent of core damage in sandwich structures and destructive methods to examine internal core damage are not viable options [3, 4]. Therefore, in order to increase weight-efficient designs using sandwich structures in the aerospace industry, it is necessary to gain a better

understanding of sandwich core behavior and expected damage modes when subjected to blunt impacts.

1.2 PRIMER ON SANDWICH PANELS

Weight reduction is a primary goal in the marine and aerospace industry, and thus, the use of sandwich structures is highly desired. Sandwich structures are materials with thin, stiff, and comparatively heavy facesheets separated by a lightweight core material [5]. These commonly include either a foam core or a honeycomb core. Although metallic materials are sometimes used, this study is particularly interested in sandwich panels with a lightweight honeycomb core and thin composite facesheets. Figure 1.2.1 [1] shows a sample configuration of the interested composite sandwich panels with a honeycomb core.

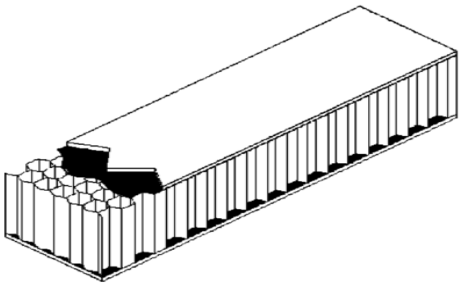

Figure 1.2.1. Sample composite sandwich panel configuation

1.3 PREVIOUS WORK

Because composite sandwich structures are vulnerable to transverse impact loads, many experimental studies were conducted to better understand the complex behavior of

the core when subjected to low velocity impacts. Significant internal damage occurred at energy levels as low as 2 J and was dependent on impact tip radius and layup of the facesheet [1]. Low velocity impacts to a composite sandwich structure resulted in barely visible damage that can reduce compressive strength up to 40%. Zonghong et al. [3] also showed that damaged panels, particularly those that exhibit core crushing, can undergo sudden fracture in the core, resulting in complete loss in load-bearing capacity and catastrophic failure. Using a drop-weight impact test, Dear et al. [6] investigated the generation of damage from onset to catastrophic failure in sandwich structures with varying facesheet materials. Thinner panels corresponded with greater overall deformation; woven glass-fiber skins were prone to puncture and core crushing while cross-plied composite skins spread impact load and minimized core crushing. Herup and Palazotto [7] showed that low-velocity impact damage is dependent on loading rate and that thick or damaged sandwiches are not quasi-static. Robinson and Davies [8] conducted impacts tests with varying impactor masses. They found that that impact damage is a function of impact energy, but not impactor mass or velocity alone. Peak force and damage size relationship is independent of specimen diameter at very low impact energies.

There has also been extensive numerical and analytical investigations on this subject. Analytical models commonly used three approaches: Hertzian contact law, energy balance, or spring-mass models [9]. Spring-mass models simplify the impactor, target panel, and supports to a system of springs and dampers. The energy balance model uses the conservation of energy to relate kinetic energy of the impactor to energy needed

to create indentations on the target panel. Other models were based on variations of Hertzian contact law to describe contact force and low velocity impact indentation damage. The contact force *F* is related to indentation damage α by:

$$\boldsymbol{F = k\alpha^n} \quad \textbf{(1)}$$

Contact stiffness *k* is given by:

$$\boldsymbol{k = \frac{4}{3}\left(\frac{R^{1/2}}{\frac{1-\nu_s^2}{E_s}+\frac{1-\nu_t^2}{E_t}}\right)} \quad \textbf{(2)}$$

In this equation, subscripts *s* and *t* represent the impactor and target panel, respectively. *R* is the radius of the impactor, *E* is modulus of elasticity, and ν is Poisson's ratio. It is important to note the dependence on impact radius and target stiffness. Higher contact force *F* is necessary to create the same indentation α for a larger radius *R*. Stiffness of the target panel $E_t$would have a similar effect. Thus, external visibility of impact damage and severity of internal damage is dependent on impact radius, and not just on the level of impact force alone.

Limited attempts were made in developing analytical models to predict the low-velocity impact response of composite sandwich structures. Olsson [10] developed an analytical model to predict impact damage caused by a large mass impactor in quasi-static conditions. This model is only applicable for large mass impacts and does not include fiber fracture. Turk and Hoo Fatt [11] derived a closed-form solution for the deformation and fracture response of composite sandwich plate using the Maximum

Stress and Tsai-Hill Criteria. This solution is applicable for static indentations with hemispherical-nose indenters. Using a two degrees-of-freedom mass-spring model, Ivañez et al. [9] developed seven dimensionless parameters that represent different factors that affect sandwich beam behavior. The resulting non-dimensional equations of motions reproduced the dynamic response of composite sandwich beams subjected to low-velocity impacts.

Many numerical analysis models have been developed to predict damage behavior before and after initial damage. Menna [12] developed a model using finite element (FE) code LS DYNA to reproduce and predict overall force-displacement curves, and the extent and shape of impact damage. This model decreases in accuracy in cases with high velocities and thick facesheets. Burman and Zenkert [2] developed a model to predict residual stiffness due to fatigue loading on undamaged and damaged honeycomb panels using a static strength notch factor. Preexisting damage may propagate until catastrophic failure under fatigue loading. However, Belingardi et al. [13] conducted fatigue analysis on honeycomb sandwich beams that suggest that prediction of fatigue strength does not apply if the failure mechanisms of the damage and undamaged specimens differed too much.

There were several studies that identify damage modes that result from low velocity impact. Othman and Barton [14] identified upper skin failure, followed by core crushing, then lower skin failure (total perforation). Abrate [15] identified six damage modes: (a) delamination in top facesheet (b) skin-core debonding (c) core crushing (d) matrix cracking (e) fiber breakage in facesheets and (f) core buckling. Mines et al. [16]

investigated static and impact behavior of sandwich beams and identified four damage modes; the first was upper skin compression failure (Mode I), upper skin crushing failure (Mode II), core shear failure (Mode III), and lower skin tensile failure (Mode IV). Most works concentrate on failure modes within the facesheets, and thus there has been less focus on impact damage modes and severity in just the core alone.

1.4 OBJECTIVES

This investigation explores impact damage formation in lightweight composite sandwich panels due to low-velocity impacts of variable tip radius and energy level. Specifically, this investigation will focus on the extent of internal core damage in cases where external damage (surface dents on top facesheet) is barely visible. External damage and visibility will be characterized quantitatively by the dent depth and span on the surface of the top facesheet of the sandwich structure. Internal core damage will be quantified by damage depth and span, and classified into various damage modes based on severity. This research will also explore the correlation between internal and external damage as a function of impact tip radius.

2 EXPERIMENTAL SETUP

2.1 PENDULUM IMPACT SYSTEM

Impact tests in this investigation were performed on a pendulum impactor, shown in Figure 2.1.1. Stainless steel masses were mounted to the end of a 1.40 m lightweight fiberglass arm, with a total mass of 3.94 to 4.72 kg depending on impact tip radius geometry. A US Digital A-2 absolute encoder with 3600 discrete steps recorded the fiberglass arm position, and allowed control of the arm angle with a 0.1° resolution. The position of the arm may then be set to correspond with the impact test potential energy. A laser photogate system was set just before the pendulum impacts the panel to record both inbound and outbound velocity. The kinetic energy can be determined to validate the desired potential energy of the test.

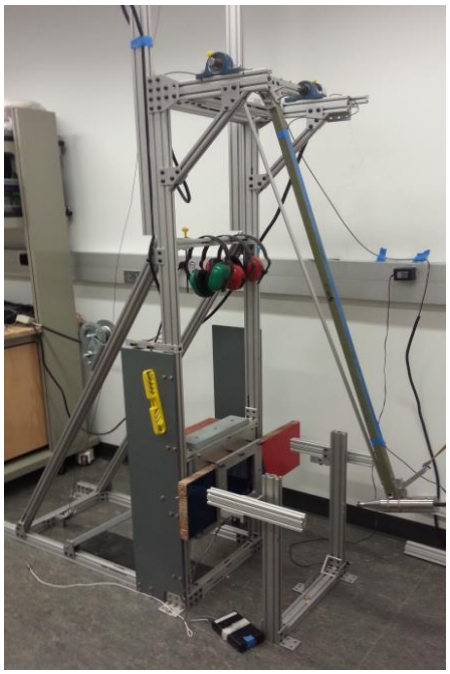

Figure 2.1.1. Pendulum Impactor

Four hardened steel impactor tips of different radii were used in this study. The radii were 12.7, 25.4, 50.8, and 76.2 mm, as shown in Figure 2.1.2. A dynamic load-cell measuring force was mounted just before the impact tip. Depending on tip size, one of two different sensors was used. Dytran model 1050V6 sensor has a conversion factor of 4.58 kN/V (provided by manufacturer), and was used with the 12.7 mm radius tip; Dytran model 1060V5 sensor has a conversion factor of 20.8 kN/V, and was used with the 25.4, 50.8, and 76.2 mm radius tips. Because the force at the point of impact differs from that measured at the transducer, a force correction factor determined by Delaney [17] was used. Figure 2.1.3 shows a close-up of the 12.7 mm tip configuration. A 12-bit USB Picoscope 3424 4-channel oscilloscope was used for all data acquisition.

Figure 2.1.2. Impact tips of radii 12.7, 25.4, 50.8, and 76.2 mm (left to right)

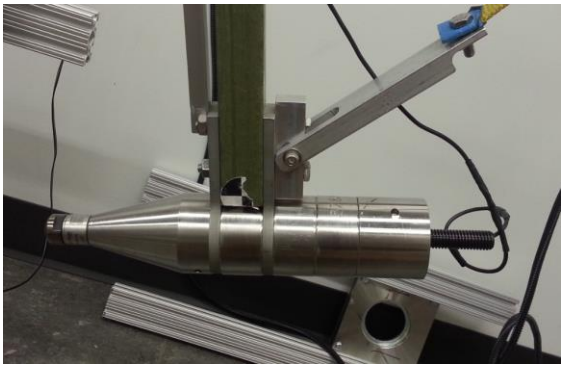

Figure 2.1.3. Close-up of impactor head configuration with 12.7 mm tip radius.

The test panels were held between two 12.7 mm thick aluminum plates with a 165 mm square window opening, as shown in Figure 2.1.4. Each test panel had a height of 210 mm with varying length, and consisted multiple test sites. Because damage in sandwich structures are highly localized, multiple impact tests may be conducted on the same panel by sliding the previous impact location beyond the fixture boundary. The front plate was only bolted on the top and bottom to allow the panel to slide through the fixture. Silicone rubber strips with 3.2 mm thickness were added between the fixture faces and the specimen to reduce bending stress concentration effects.

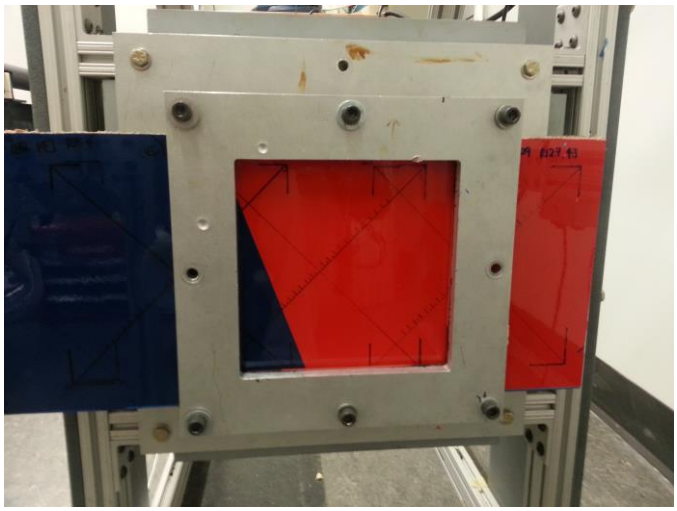

Figure 2.1.4. Front view of test panel fixture.

2.2 Test Specimens

The test specimens used in this investigation were composite sandwich panels with a Nomex honeycomb core obtained from an Airbus A320 rudder. Figure 2.2.1 shows a side view of the test specimen and a top view of the core (with facesheets

removed). The front (outward facing) facesheet had an average thickness of 1.19 mm (including paint); the average back facesheet thickness was 0.64 mm. Average core thickness was 29.4 mm, with an approximate core density of 35 kg/m^3 and cell size of approximately 5.2 mm.

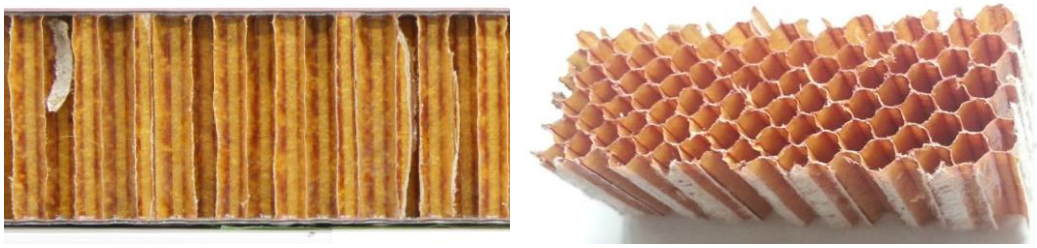

Figure 2.2.1. Side (L) and top (R) view of test panels

Using a resin burn-off method, in which a small specimen of the top and bottom facesheet was placed in a tube furnace and heated to above 450 ^{o}C for 30 minutes, the layup of the top and bottom facesheets were determined to consist of two plies. The inner layer contacting the honeycomb core was plain weave fiberglass, while the outer layer is carbon fiber with a [45/-45] and over two under one weave configuration. The two layers are pictured in Figure 2.2.2.

Figure 2.2.2. Inner fiberglass layer (L) and outer carbon fiber layer (R) of top and bottom facesheets

2.3 Experimental Procedure

For each impact test, the test panel was slid into the fixture such that previous test sites were outside of the window opening. The top and bottom bolts were only hand-tightened so that honeycomb core will not experience crushing. The requisite pendulum arm angle was calculated to correspond to the desired potential energy level. These calculations were based on previous work done by Delaney [17] and are documented in Appendix IV. The pendulum arm was secured to a pneumatic locking mechanism and then raised to the appropriate position. Pressurized air was directed to the mechanism, and the pendulum arm was released. Each test site was subjected to only a single impact.

After each impact, the panel was immediately removed from the fixture for dent depth measurement using a Mitutoyo model ID-S1012E depth indicator. Measurements were recorded every 6.35 mm starting at the point of impact to +/- 76.2 mm on either side of the center point to create an immediate dent profile. The maximum dent depth was determined adjusting the measurements with a linear slope correction. Because sandwich panels tend to experience relaxation over time, this process was repeated after 24 hours to document a relaxed dent profile and relaxed dent depth. The span of the dent was determined using the dent profile. Force and velocity data were extracted using the MATLAB code included Appendix IV.

Each test site was then sectioned and lightly polished to remove extraneous fibers from the core walls for a clear view of its internal damage. The core damage depth was measured from the neutral axis. The span of the core damage was also measured. The core was closely examined to determine damage modes present.

3 RESULTS

3.1 TEST SUMMARY AND MATRIX

For this experimental study, 32 impact tests were conducted using impact tips with radii of 12.7, 25.4, 50.8, and 76.2 mm at energy levels ranging from 2 to 14 J. The number of tests performed at each radius and energy combination is summarized in Table 3.1.1. Appendix I lists each test, labeled LVS-0XX, with their corresponding information and test data. This includes inbound/outbound kinetic energy, maximum impact force, immediate/relaxed dent depth, and visibility.

Table 3.1.1. Number of tests conducted at each radius/energy combination

R (mm)	2 J	4 J	6 J	10 J	14 J
12.7	2	2*	1*	-	-
25.4	2	3	2	1	1*
50.8	2	3		1	1
76.2	2	3	2	-	1

* Numbers with asterisks indicates tests that resulted in a cracked facesheet.

3.2 DATA ACQUISITION

For each test, two sets of data were saved using the Picoscope data acquisition system. The first set contains voltage information from the laser photogate system. The voltage remained at 2 V when the laser path was clear; when the laser path was obstructed as the pendulum passed through, the voltage increased to 8 V. Using this time

duration and the width of the pendulum arm passing through the laser photogate, the inbound and outbound velocity information may be calculated to determine their respective kinetic energies. Figure 3.2.1 shows an example of this photogate data recorded in the case of a 4 J impact using a 50.8 mm radius tip. The inbound velocity was 1.41 m/s and the outbound was 0.86 m/s

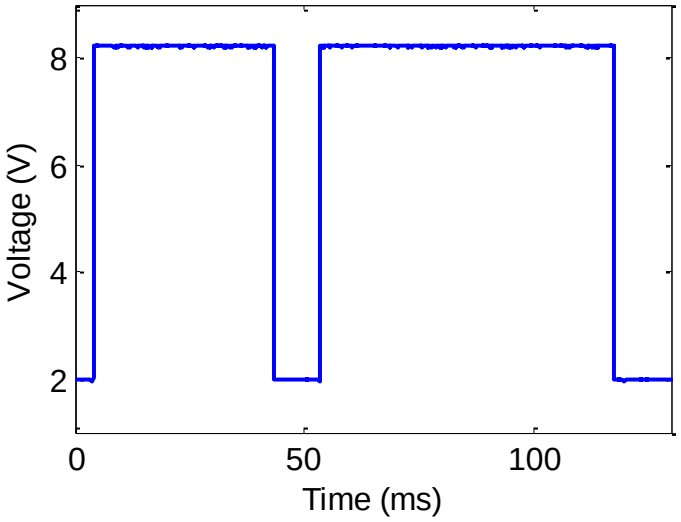

Figure 3.2.1. Inbound and outbound laser voltage data for test LVS-016 (R50.8 mm at 4 J)

The second set of data recorded voltage information from the dynamic force sensor mounted just aft of the impactor tip. Using the conversion factor provided by the manufacturer and the force correction factor found by Delaney [17], the voltage information was converted to force. The force vs. time curve for test LVS-016 can be seen in Figure 3.2.2. This relatively smooth curve is representative of impact tests in which there was no cracking or penetration of the sandwich panel's top facesheet. In

cases where the top facesheet exhibited cracking or penetration damage, the curve increased smoothly before experiencing a sudden drop in force. This can be seen in Figure 3.2.3 where the R25.4 mm tip cracked the top facesheet in a 14 J impact test.

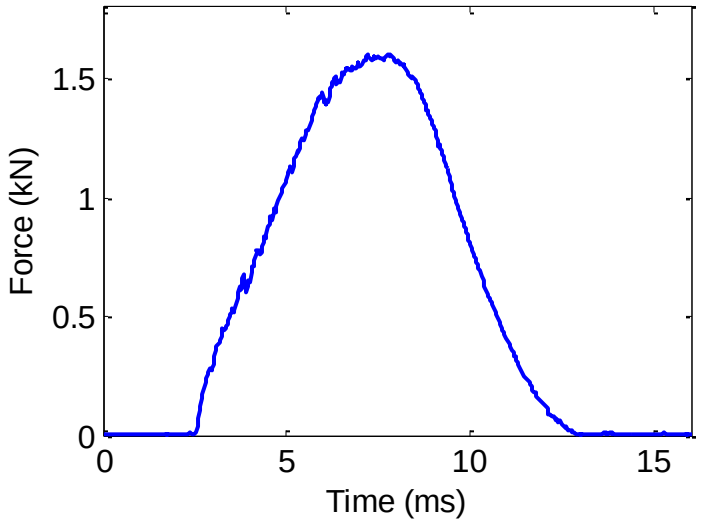

Figure 3.2.2. Force vs time history data for test LVS-016 (R50.8 mm at 4 J); no cracking in facesheet

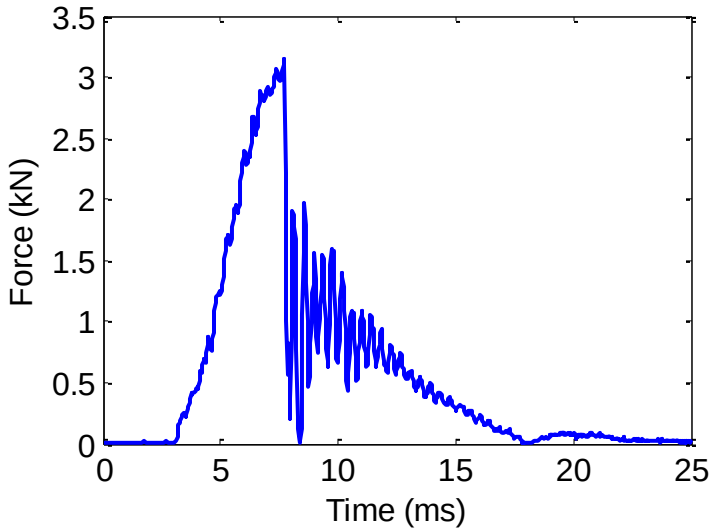

Figure 3.2.3. Force vs time data for test LVS-032 (R25.4 mm at 14 J); cracked facesheet

3.3 Immediate and Relaxed Dent Depths

Immediately after impact, the panel was removed from the fixture for dent depth measurement. Measurements were recorded at 6.35 mm intervals (1/4") up to 76.2 mm on either side of the center of impact. Because the facesheet's bending stiffness has a restoration effect on the core, this process was repeated 24 hours later to obtain a relaxed dent profile. The two profiles for test LVS-016 can be seen in Figure 3.3.1. As expected, dent damage was highly localized. In the case of LVS-016, in which the panel was impacted at 4 J with a 50.8 mm radius tip, the maximum dent depth immediately after impact was 0.58 mm. The sandwich panel began to relax very quickly after impact. As seen in Figure 3.3.2, where the dent depth is plotted as a function of time, the test site was fully relaxed after 2 hours with a relaxed dent depth of 0.55 mm. It should be noted that although the depth indicator has a resolution of 0.01 mm, actual accuracy may be lower due to variability in the small depths measured.

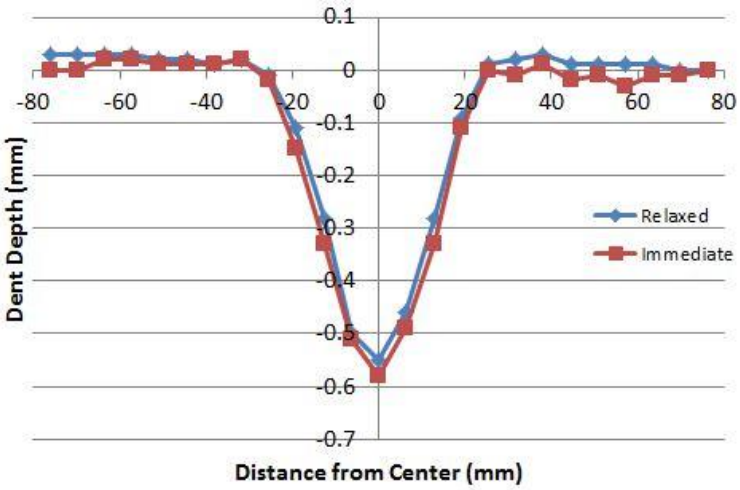

Figure 3.3.1. Dent profile of test LVS-016 (R50.8 mm at 4 J)

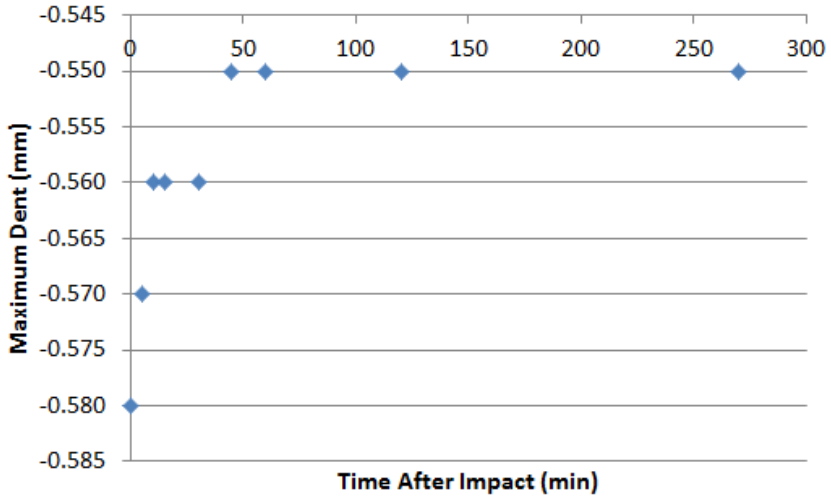

Figure 3.3.2. Time history of maximum dent depth for test LVS-016 (R50.8 mm at 4 J)

A plot of the relationship between measured kinetic energies and immediate maximum dent depth can be seen in Figure 3.3.3. The correlation between dent depth and kinetic energy was fairly linear in the lower energy levels up to 6 J. All points seemed to overlap regardless of the four different tip radii in the lower energy range (up to 6 J). At higher energies of 10 to 14 J, the dent depths varied considerably for the different radii, suggesting that the depths increase at different rates with increasing impact energy. In most cases, the panel experienced only surface dent damage. The four outlying points (filled-in points in the plot) are instances where the facesheet was cracked. These instances occurred only in impact test with tip radius 12.7 mm (diamond) and 25.4 mm (square).

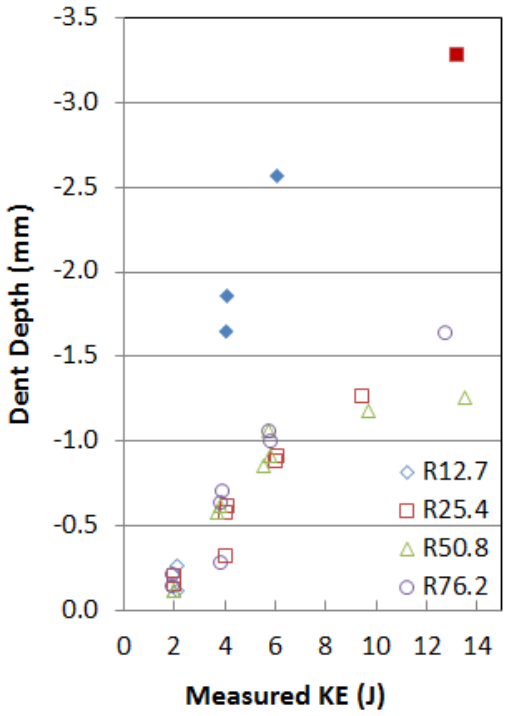

Figure 3.3.3. Maximum dent depth vs. measure kinetic energy level

These dents exhibited very low levels of relaxation; most dents relaxed less than 10 percent of the immediate depth, while several approached 20 percent. The only instance where relaxation exceeded 20 percent, indicated by the filled-in data point in Figure 3.3.4, occurred in cases of lower impact energy with very small dent depths (~0.10 mm). Variability in these very small depth measurements had a large impact on relaxation percentage, resulting in a dent relaxation that is considerably higher than the remaining cases. Although relaxation is generally low, it is still necessary to report impact damage immediately after it occurs since the shallow dents may not be easily detected in future inspection because of its barely visible nature.

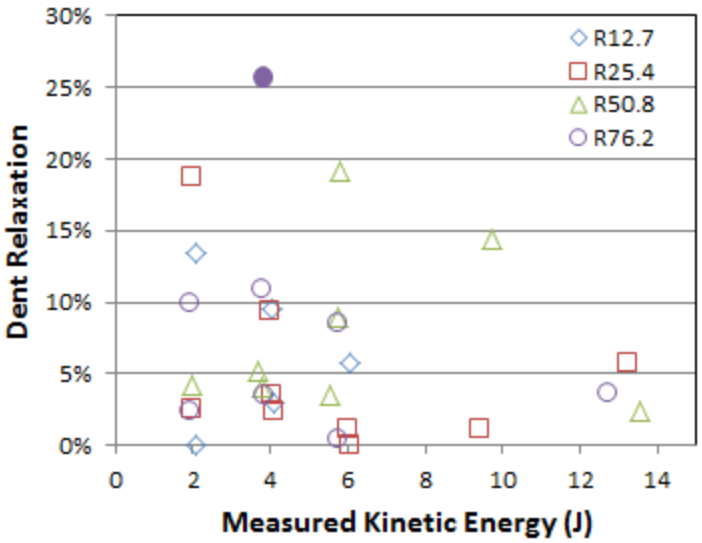

Figure 3.3.4. Level of dent relaxation

3.4 Visibility of Dent Damage

The depth of a dent is a common measurement used to indicate the extent of impact damage, but it cannot be the sole basis used to characterize external damage. In this study, the visibility of the dent was quantified based on a parameter defined as the maximum depth D divided by the dent span S. Dent span S was determined as the span of the dent at one-third of the depth below the original surface plane, as shown in Figure 3.4.1. Because visual detectability of damage is dependent on both span and depth, this parameter is more indicative of its visibility than depth alone.

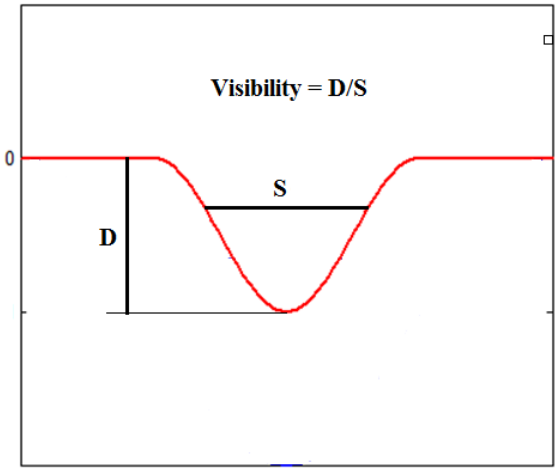

Figure 3.4.1. Visibility paramater as ratio of depth/span

Figure 3.4.2 shows this visibility parameter as a function of measured kinetic energy. Because this study is primarily interested in events where external damage is barely visible, cases in which the surface experienced cracking (and thus having high visibility) were excluded from this plot. In general, surface dents resulting from impact tip radius 50.8 mm had significantly lower visibility (depth/span) compared to those due to other tip radii at similar energy levels. Visibilities of dents created by R76.2 and R25.4 mm were both higher than that of R50.8 mm; however, visibility values from these two radii tend to fall on a common curve over the range of energy tested. Thus, although visibility increased with kinetic energy, there was no clear relationship with the different tip radii.

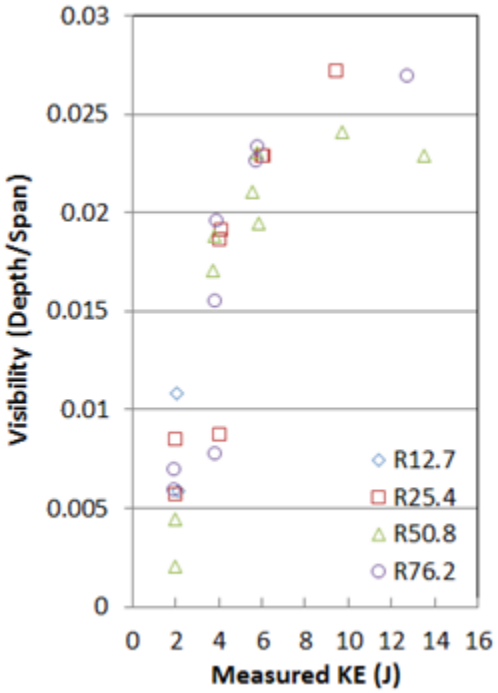

Figure 3.4.2. Visibility (D/S) of surface dents as function of kinetic energy

3.5 Energy Dissipation

The inbound and outbound velocities of each test were compared to determine the amount of energy dissipated by the test panel during each impact. In cases where there was no surface cracking, the amount of energy dissipated ranged from 55 to 70 percent. Two trends are visible in Figure 3.5.1. In the lower range of energies tested (from 2 to 6 J), energy absorbed from a R25.4 mm radius tip was in the lower end of this range while R76.2 mm was at the higher end, and remained at a fairly constant level. This was expected, since a sharper tip correlates to lower contact area, resulting in less energy absorption. As impact energy increased to 10 and 14 J, the amount of energy absorbed

began to increase at different rates. Figure 3.5.1 suggests that less energy is dissipated when impacted by sharper tips (such as the R25.4) than blunter tips (such as the R50.8 and R76.2), but increase more quickly, resulting in surface cracking damage sooner than their blunt counter-parts. Filled in data points on the plot are instances where the facesheet was also cracked.

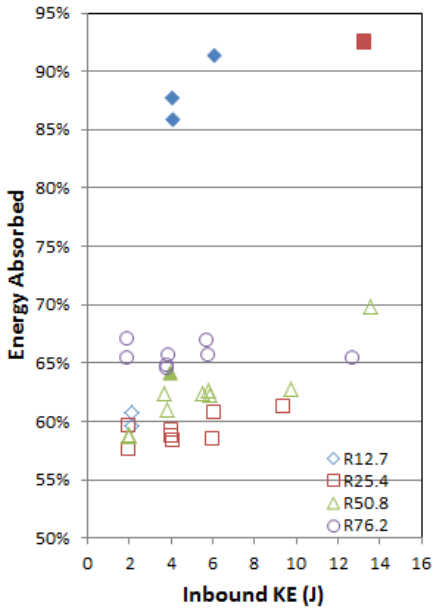

Figure 3.5.1. Energy dissipated by test panel

3.6 Internal Damage Modes

Each test site was destructively sectioned (cut through the center point of impact) to observe damage to the honeycomb core. The cross-sectional inspections and additional optical microscope observations were used to identify four distinct modes of internal damage to the Nomex honeycomb core. These modes were identified as:

- Mode A: Slight wrinkling of cell walls, visible only with application of additional applied pressure (see Figure 3.6.1)
- Mode B: Visible wrinkling of cell walls without applied pressure (see Figure 3.6.2)
- Mode C: Buckling/Kinking of cell walls; similar to mode B but more severe (see Figure 3.6.2)
- Mode D: Fiber fracture and/or bursting of cell walls (see Figure 3.6.3)

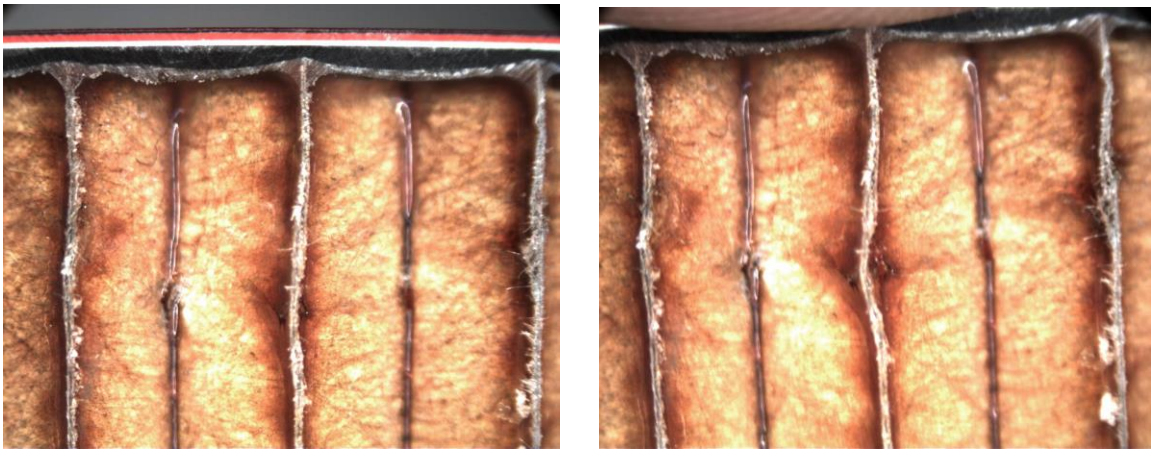

Figure 3.6.1. Damage mode A without applied pressure (L) and with applied pressure (R)

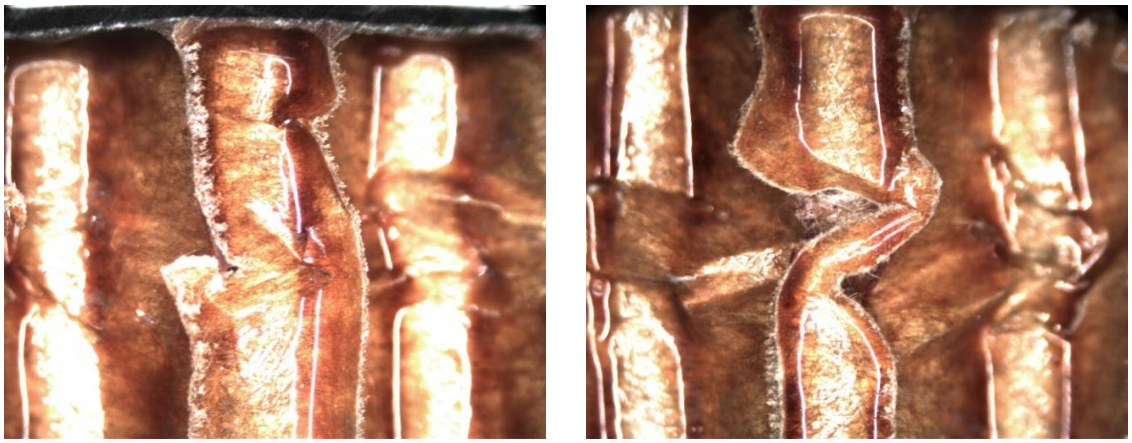

Figure 3.6.2. Damage modes B (L) and C (R)

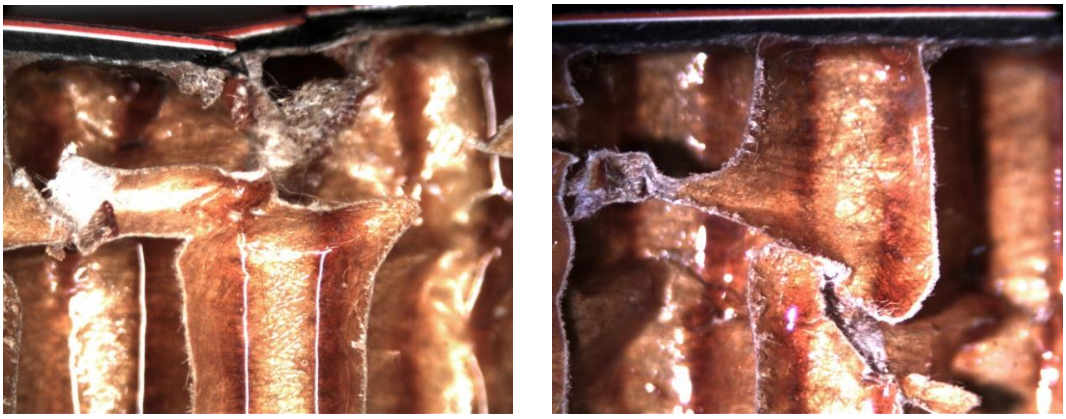

Figure 3.6.3. Damage mode D with surface cracking (L) and only dent damage (R)

Each test site was inspected and the damage modes present in each were documented. In all cases, the presence of a higher damage mode corresponded with the existence of all lower damage modes. Figure 3.6.4 shows the cross section of test LVS-033 where the panel was impacted with a R76.2 mm tip at a target energy of 14 J and exhibits all four damage modes identified. The most severe damage (Mode D) occurs in the center, directly below the point of impact, and decreases in severity as it moves further from the centerline.

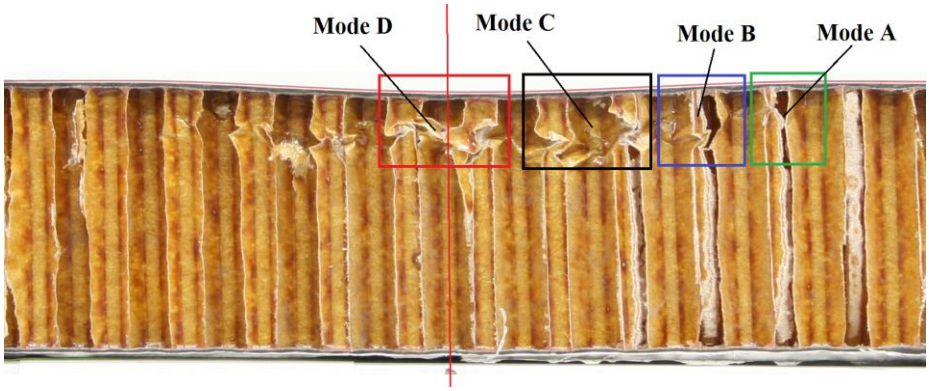

Figure 3.6.4. Cross-section of test LVS-033 with all four damage modes present

Tables 3.6.1 through 3.6.4 summarize the damage modes observed in each test site due to different radii impact tips. Damage mode A occurred for all tip radii at all energy levels tested. Damage mode B occurred in tests with impact energy levels as low as 2 J for the sharper tips R12.7 mm and R 25.4 mm. In the cases with the blunter tips, R50.8 mm and R76.2 mm, mode B did not develop until higher energies. Mode C did not appear in R76.2 mm tests until 6 J and higher. Similarly, mode D developed at higher energies for increasing tip radius. For R76.2 mm, mode D was not observed until 12.72 J. This indicates a clear relationship between core damage severity and tip radius; In general, a sharper tip results in more localized and more severe damage at lower energy levels, while blunter radius tip requires significantly higher energy levels to produce more severe damage modes (C and D).

Table 3.6.1. Summary of damage modes present in test sites impacted with R12.7 mm tip

Test No.	KE_In (J)	Mode A	Mode B	Mode C	Mode D
LVS-006	2.08	x	x		
LVS-030	2.09	x	x		
LVS-029	4.05	x	x	x	x
LVS-008	4.08	x	x	x	x
LVS-007	6.07	x	x	x	x

Table 3.6.2. Summary of damage modes present in test sites impacted with R25.4 mm tip

Test No.	KE_In (J)	Mode A	Mode B	Mode C	Mode D
LVS-023	1.99	x	x		
LVS-024	1.99	x	x		
LVS-025	4.00	x	x		
LVS-022	4.03	x	x		
LVS-026	4.08	x	x	x	
LVS-020	6.02	x	x	x	
LVS-021	6.08	x	x	x	
LVS-031	9.41	x	x	x	x
LVS-032	13.23	x	x	x	x

Table 3.6.3. Summary of damage modes present in test sites impacted with R50.8 mm tip

Test No.	KE_In (J)	Mode A	Mode B	Mode C	Mode D
LVS-018	1.97	x			
LVS-019	1.99	x			
LVS-016	3.70	x	x	x	
LVS-027	3.80	x	x	x	
LVS-002	3.95	x	x	x	
LVS-017	5.54	x	x	x	
LVS-028	5.75	x	x	x	
LVS-003	5.83	x	x	x	
LVS-004	9.72	x	x	x	x
LVS-005	13.54	x	x	x	x

Table 3.6.4. Summary of damage modes present in test sites impacted with R76.2 mm tip

Test No.	KE_In (J)	Mode A	Mode B	Mode C	Mode D
LVS-014	1.90	x			
LVS-015	1.91	x			
LVS-013	3.81	x	x		
LVS-010	3.83	x			
LVS-011	3.85	x	x		
LVS-009	5.73	x	x		
LVS-012	5.77	x	x	x	
LVS-033	12.72	x	x	x	x

The honeycomb core in sites impacted with the R50.8 mm tip displayed more severe damage than those impacted by the R76.2 and R25.4 tips, as seen in the cross-sections of Figure 3.6.5. This behavior is unexpected and suggests a possible interaction between maximum damage behavior, and the cell size of the core. However, this relationship remains an area for future investigations.

Figure 3.6.5. Cross section of tests LVS-022, 027, and 010 impacted at 4 J with increasing tip radii

Facesheet cracking was always accompanied by damage mode D (core wall fracture). However, the opposite was not always true; core wall fracture (mode D) may occur when external damage only includes a shallow dent (no facesheet penetration). This was seen in impacts with blunter tips R50.8 mm and R76.2 mm at energy levels above 6 J. There was no surface cracking for R50.8 mm at 10 and 14 J or for R76.2 mm at 14 J. However, close examination of their cross-sections revealed fiber breakage

directly below the point of impact. Even small fractures in the honeycomb core may serve as seed damage which can affect the facesheet separation under repeated cyclic loading during an aircraft's ground-air-ground cycle. Thus, the existence of damage mode D in cases where there is no external indicator is a large threat to aircraft structural integrity. Visual inspection of dents in sandwich structures is not always an accurate indicator of core damage severity. There is a need for further understanding and better methods to detect such damage modes in the sandwich substructure.

3.7 Internal Depth and Span

The damage span and depth in the core was measured for each test site. These measurements included parts of the core exhibiting any sign of damage (Modes A through D). An example of overall and main damage span is shown in Figure 3.7.1. As expected, and seen in Figure 3.7.2, the internal damage span increased with increasing impact energy. At the lower energy levels of 2 to 6 J, the spans overlap, indicating there is little dependence of damage span based on impact tip radii. However, when impact energies were increased beyond 6 J, the spans varied considerably more. The plots suggest that the damage span could plateau with increasing energy (e.g., see R25.4 mm and R50.8 mm data points), but more tests in the relatively higher energy range would be necessary to be certain.

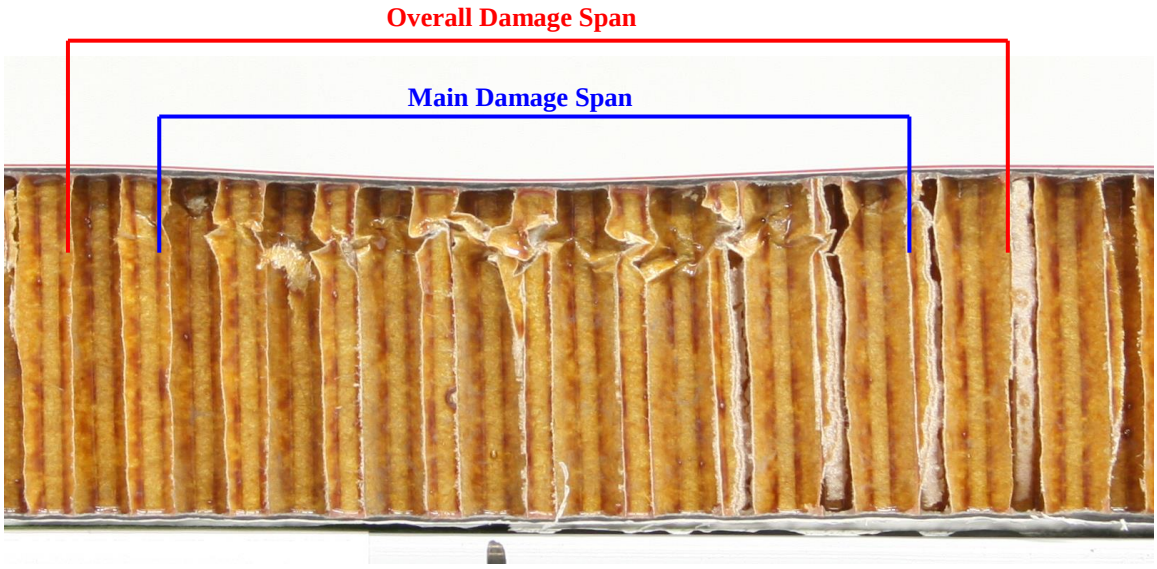

Figure 3.7.1. Overall and main internal damage span

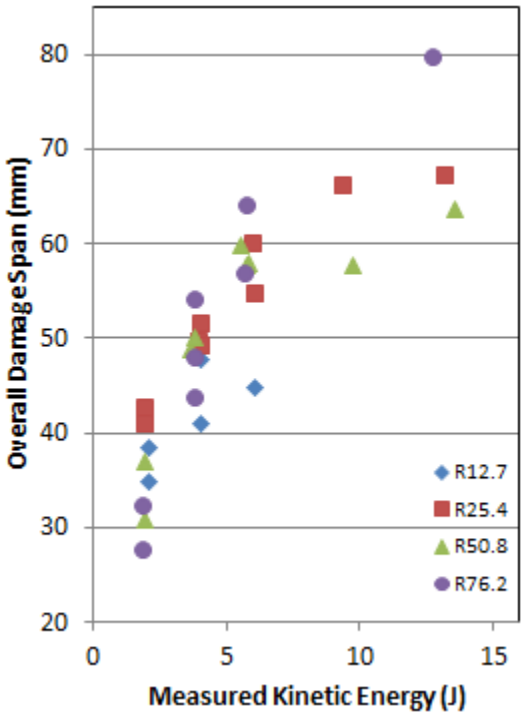

Figure 3.7.2. Internal overall damage span with increasing kinetic energy

However, when the main damage span as determined by the existence of the more severe damage modes B through D (where mode A is not considered), as shown in Figure 3.7.3, the different tip radii exhibited clear trends and variability. Data points for R12.7 were omitted since they are all cases that exhibited facesheet cracking.

At 2 J, the main damage span due to R76.2 mm impacts was the smallest of all energy levels tested. Only damage mode B was present in the center of impact. The span for R76.2 mm tip increases at a higher rate than the other radii tips such that it had the largest span at 14 J. The spans increased approximately linearly at a similar rate for impacts from tip radii R25.4 and R50.8 mm. There is significantly more scatter in the data associated with the R76.2 tip.

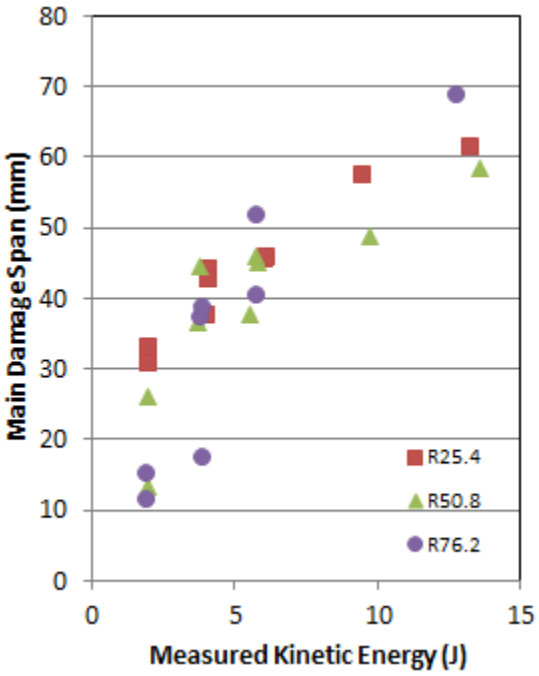

Figure 3.7.3. Internal main damage span (modes B through D) with increasing kinetic energy

The main internal damage spans at similar impact energy levels did not increase with increasing tip radii as expected. The spans from the R50.8 tip were consistently lowest, followed by R25.4 with the longest spans. Although internal damage due to the R50.8 tip displayed more severe damage modes at lower energy levels than R25.4, as seen in Table 3.6.3, the main damage span was lower. There was more damage concentration in the center for R50.8 than for R25.4 or R76.2 despite its generally shorter internal damage span. This unexpected behavior of the core due to R50.8 tip impacts may be due to an "optimal" damage relationship with core cell size. This remains an area for future study.

The extent of internal damage was also observed and quantified using its damage depth. The damage depth was determined with respect to the neutral surface plane (original undamaged facesheet surface) of the panel, and measured the depth of core damage, as shown in Figure 3.7.4. Two types of damage depths were investigated. The overall damage depth was measured from the neutral plane to the furthest point in the core where any evidence of wrinkling was present, and no damage was observed below that point. There is no clear dependence on impact energy, as evident in Figure 3.7.5. Although the damage depth seems to vary with tip radii, there is too much scatter in the data to identify clear trends.

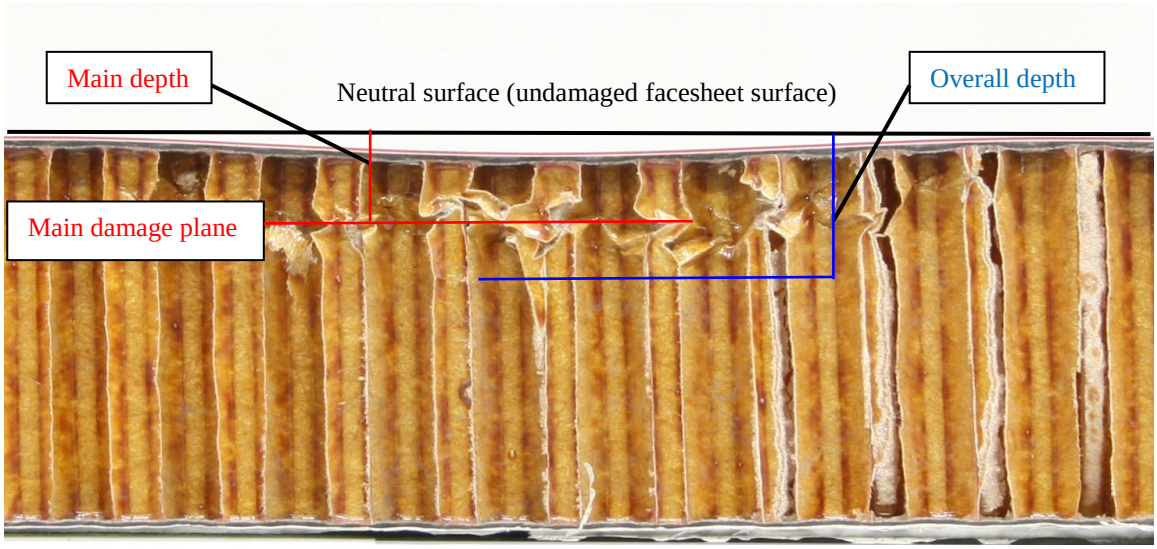

Figure 3.7.4. Overall and main internal damage depth

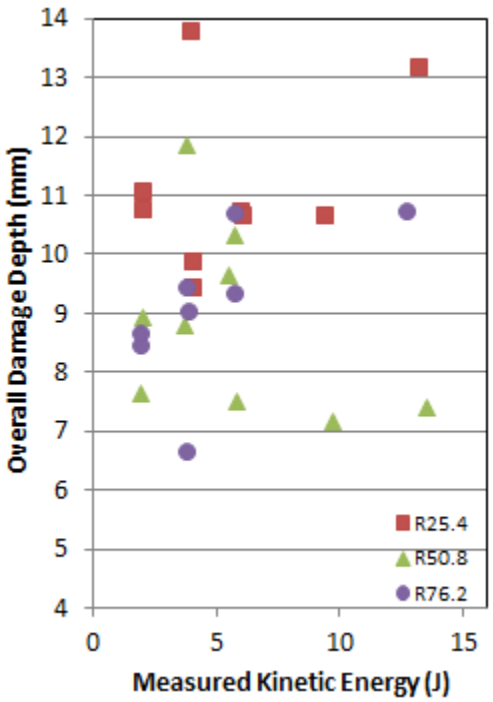

Figure 3.7.5. Internal overall damage depth with increasing kinetic energy

When the main damage depth was measured from the neutral surface plane (original undamaged facesheet surface) to the main damage plane of core damage (where depth plateaued) as shown in Figure 3.7.4, scatter was reduced as visible in Figure 3.7.6. Damage depth plateaus to a very narrow range for each impact tip and is independent of impact energy. In general, damage depth due to impact tip R50.8 is lowest, followed by R76.2 and R25.4. Damage due to R12.7 tip were omitted due to facesheet damage.

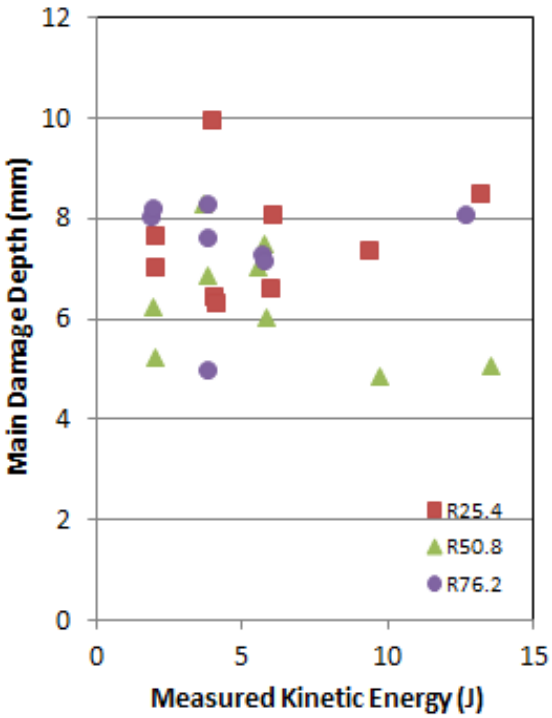

Figure 3.7.6. Main damage depth with increasing kinetic energy

Internal damage in terms of span and depth due to increasing energy can be more clearly seen in the damage progression for impact tip R25.4 in Figure 3.7.7. Damage span increases with increasing impact energy, but damage depth quickly plateaus to a damage

plane that is independent of impact energy. Damage progression for the other tips can be found in Appendix IIIa.

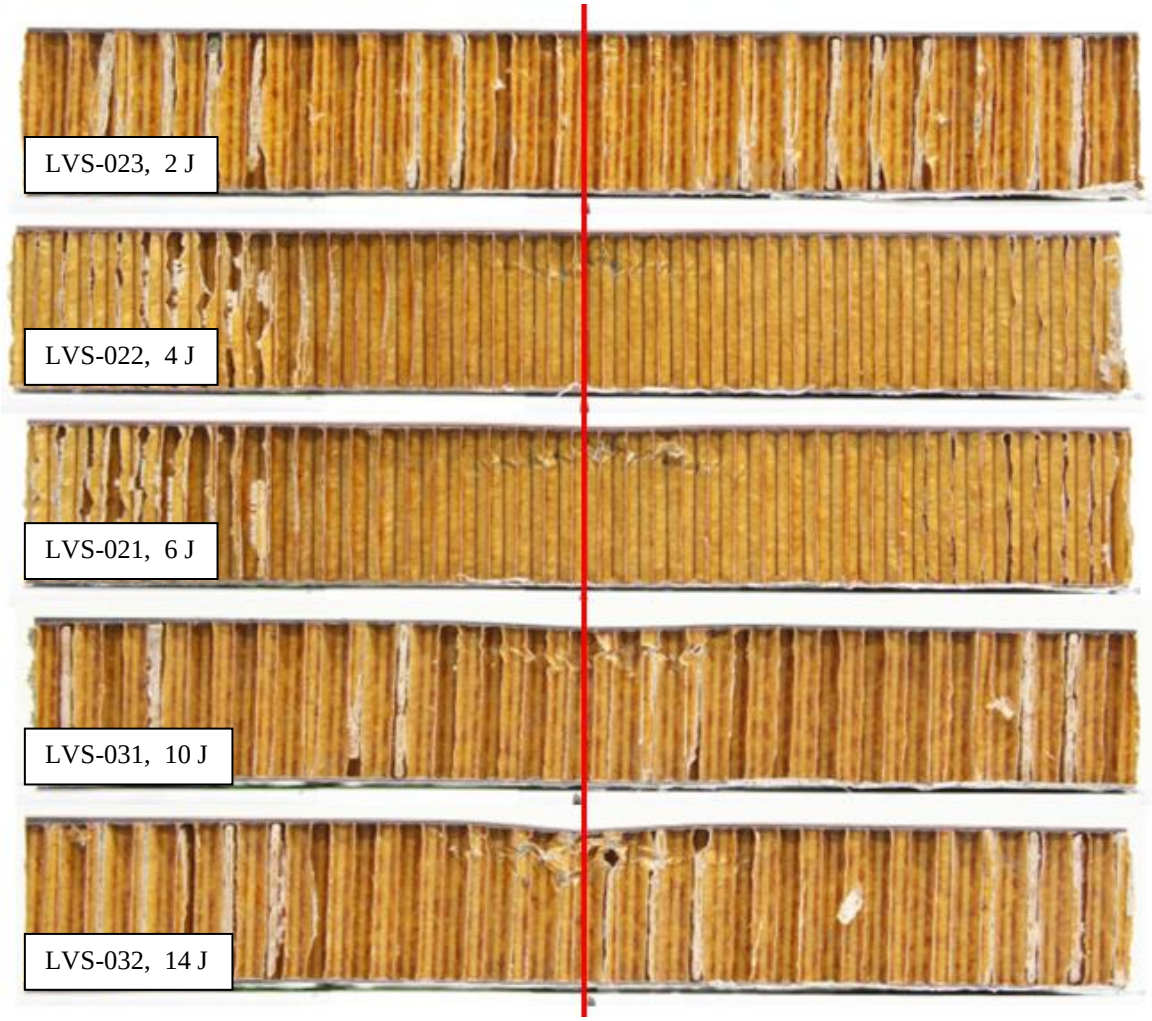

Figure 3.7.7. Damage progression with increasing kinetic energy (2, 4, 6, 10, 14 J) for R25.4

The damage depth cannot be determined by external visual inspection. While the damage span increases with increasing external visibility, as shown in Figure 3.7.8, there is no correlation for damage depth. The damage depth remains in a narrow range

regardless of visibility. This depth range is hypothesized to be a function of the core wall and cell size geometry. Similarly, the damage span increases fairly linearly with increasing dent span, as shown in Figure 3.7.9, suggesting that external dent span is a good indicator of internal damage span. The dotted line shows a 1:1 relationship, showing that the internal span damage is larger than the externally-observable span. However, damage depth remains in a narrow range regardless of external dent depth. Thus, internal damage depth cannot be predicted based on external observations.

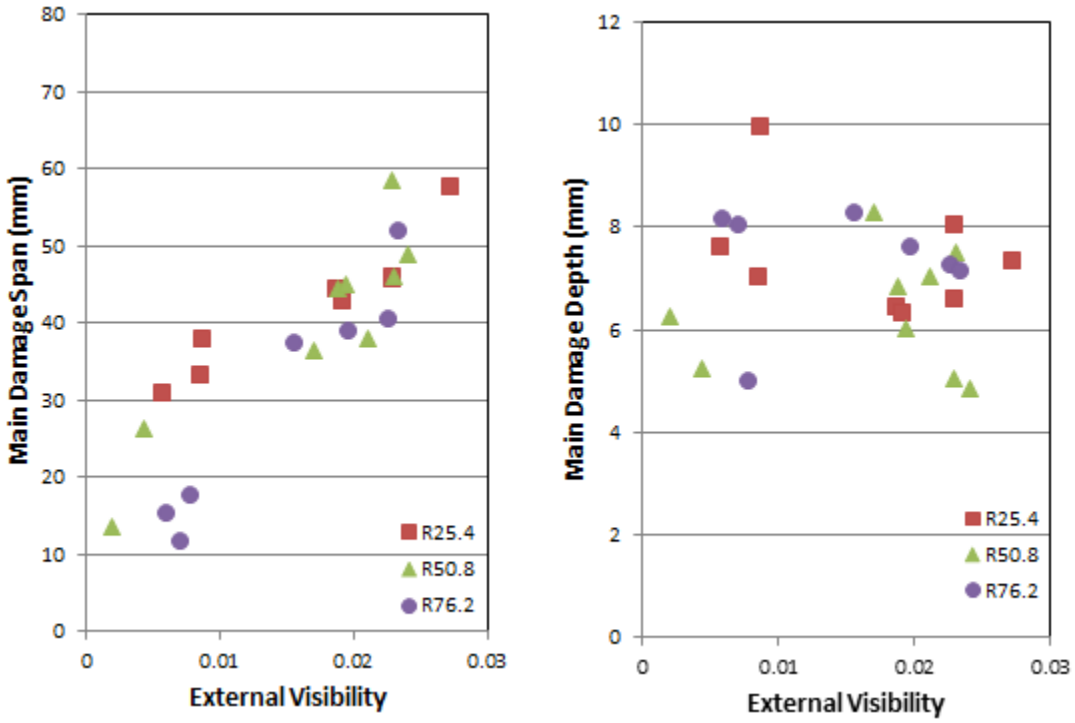

Figure 3.7.8. Internal damage span (L) and depth (R) with increasing external visibility

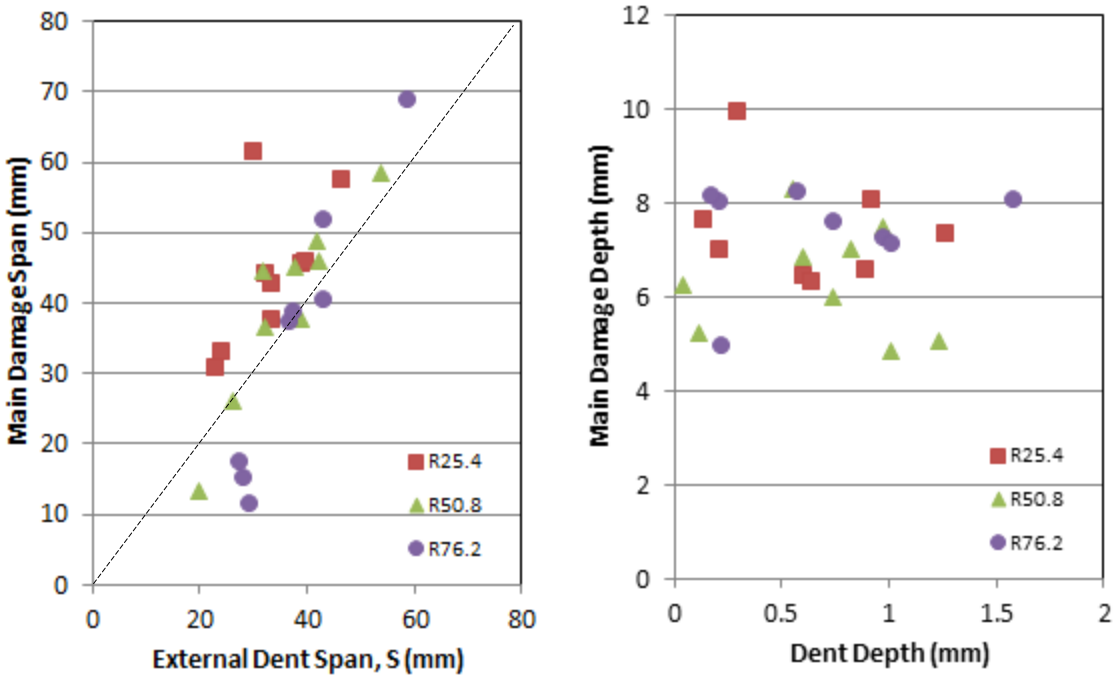

Figure 3.7.9. Internal damage span (L) and depth (R) compared with external damage

4 DISCUSSION AND CONCLUSIONS

Composites are increasingly common in the aerospace industry. There is a growing desire to incorporate more composite sandwich structures in order to increase stiffness without significant increase in structural weight. Thus, it is necessary to understand the extent of internal core damage due to impact loading, especially in cases where external damage is just barely visible. This experimental investigation explores the external and internal damage morphology in sandwich panels subjected to low velocity impacts. The sandwich panels were impacted with tip radii 12.7, 25.4, 50.8, and 76.2 mm at energy levels ranging from 2 to 14 J.

Visual inspection of dents is traditionally used to assess damage in metallic structures. However, this method is not as effective when applied to composite sandwich structures. The facesheet's bending stiffness generally has a restoration effect on the core, causing dents to relax after impact. Relaxation in this investigation was very low and has an insignificant effect on maximum dent and visibility.

The span of the external dent was measured and related to its dent depth to quantify a visibility parameter. Visibility increased with increasing impact energy, but was independent of impact tip radius for the range of energy studied. In cases where there was no cracking of the facesheet, dent damage was very shallow and difficult to detect. Damage due to these low velocity impact events may be easily overlooked when inspecting a large structure. Knowledge of the general impact location and close examination would be necessary in order to detect these dents. Thus, it is urgent to report an impact event soon after occurrence because visual detectability is very low. Since

visibility is independent of tip radii in lower energies, it is more important to know the energy with which the area was impacted. The projectile radius itself, although necessary to gain a general assessment of the damage, has a less significant effect. In practice, the radius of the impacting object may be difficult to determine due to its many possible orientations.

Internal damage span increased with increasing impact energy as well as increasing external visibility. Thus, knowing the visibility (dent span and depth) would provide a good estimate of the internal damage span. However, this is not the case for internal damage depth. The damage depth was independent of both energy and visibility, indicating that traditional methods of visual inspection of damage are insufficient to characterize core damage. Furthermore, the most severe damage mode observed (Mode D), where core walls exhibited fracture, was not always accompanied by facesheet cracking and cannot be visually detected without sectioning the panel. Thus, the usefulness of external damage inspection and visibility is questionable, as it does not accurately reflect the extent of internal damage in lightweight honeycomb sandwich panels.

Furthermore, the internal damage depth of the core was lowest for impacts with tip radius 50.8 mm. Higher damage modes also occurred at lower impact energy for this tip as well. Thus, damage was more severe, but occurred closer to the facesheet, than that due to both the blunter 76.2 and sharper 25.4 mm tips. Internal damage span did not increase with increasing tip radii, and internal damage depth did not increase with decreasing tip radii as expected. This suggests that there is a relationship between core

density/cell size and maximum damage behavior due to an “optimal” tip radius. Tip radius 50.8 mm was the “optimal” tip in this investigation.

Future work could seek to explain some of the observations made in this study. The correlation between damage due to an optimal tip radius and core cell size should be explored. Residual strength testing of sandwich structures with various degrees of core span and depth damage may be done to determine structural performance reduction. Further understanding of the complex internal core behavior as it relates to impact energy and radius is necessary to develop a more efficient method of determining damage in sandwich structures.

WORKS CITED

[1] M. Meo, R. Vignjevic and G. Marengo, "The response of honeycomb sandwich panels under low-velocity impact loading," *International Journal of Mechanical Sciences*, vol. 47, no. 9, pp. 1301-1325, 2005.

[2] M. Burman and D. Zenkert, "Fatigue of Undamaged and Damaged Honeycomb Sandwich Beams," *Journal of Sandwich Structures and Materials,* vol. 2, no. 1, pp. 50-74, 2000.

[3] X. Zonghong, A. Vizzini and T. Qingru, "On residual compressive strength prediction of composite sandwich panels after low-velocity impact damage," *Acta Mechanica Solida Sinica*, vol. 19, no. 1, pp. 9-17, 2006.

[4] M. S. Hoo Fatt and K. S. Park, "Dynamic models for low-velocity impact damage of composite sandwich panels – Part A: Deformation," *Composite Structures,* vol. 52, no. 3-4, pp. 335-351, 2001.

[5] N. Chakraborty, V. Rathod, D. R. Mahapatra and S. Gopalakrishnan, "Guided wave based detection of damage in honeycomb core sandwich structures," *NDT&E International,* vol. 49, pp. 27-33, 2012.

[6] J. Dear, H. Lee and S. Brown, "Impact damage processes in composite sheet and sandwich honeycomb materials," *International Journal of Impact Engineering,* vol. 32, no. 1-4, pp. 130-154, 2005.

[7] E. Herup and A. Palazotto, "Low-velocity impact damage initiation in graphite/epoxy/Nomex honeycomb-sandwich plates," *Composites Science and Technology,* vol. 57, pp. 1581-1598, 1997.

[8] P. Robinson and G. Davies, "Impactor mass and specimen geometry effects in low velocity impact of laminated composites," *International Journal of Impact Engineering,* vol. 12, no. 2, pp. 189-207, 1992.

[9] I. Ivañez, E. Barberi and S. Sanchez-Saez, "Analytical study of the low-velocity impact response of composite sandwich beams," *Composite Structures,* vol. 111, pp. 459-467, 2014.

[10] R. Olsson, "Analytical prediction of large mass impact damage in composite laminates," *Composites: Part A,* vol. 32, no. 9, pp. 1207-1215, 2001.

[11] M. H. Turk and M. S. Hoo Fatt, "Localized damage response of composite sandwich plates," *Composites: Part B,* vol. 30, pp. 157-165, 1999.

[12] C. Menna, A. Zinno, D. Asprone and A. Prota, "Numerical assessment of the impact behavior of honeycomb sandwich structures," *Composite Structures,* vol. 106, pp. 326-339, 2013.

[13] G. Belingardi, P. Martella and L. Peroni, "Fatigue analysis of honeycomb-composite sandwich beams," *Composites: Part A,* vol. 38, no. 4, pp. 1183-1191, 2007.

[14] A. Othman and D. Barton, "Failure initiation and propagation characteristics of honeycomb sandwich composites," *Composite Structures,* vol. 85, no. 2, pp. 126-138, 2008.

[15] S. Abrate, Impact on Composite Structures, Cambridge: Cambridge University Press, 1998, pp. 242-57.

[16] R. Mines, C. Worrallt and A. Gibson, "The static and impact behaviour of polymer composite sandwich beams," *Composites,* vol. 25, no. 2, pp. 95-110, 1994.

[17] M. Delaney, "Low Velocity Impacts on Composite Structures," M.S. thesis, University of California, San Diego, La Jolla, CA, United States, 2012.

APPENDICES

Test No. (LVS-XXX)	Date	Tip Radius (mm)	Pendulum Height (m)	Potential Energy (J)	Pendulum Head Veolc. In (m/s)	System Total Mass (kg)	Actual KE In (J)	Actual KE Out (J)	Peak Force (kN)	Actual In Veloc. (m/s)	Actual Out Veloc. (m/s)	e= Vout/Vin	Visible Dmg (Y/N)	Max Dent Depth (mm)	Max Relaxed Dent (mm)	Relaxation	Visbility (Immediate)	Visbility (Relaxed)
LVS-001	4/17/2013	50.8	0.0996	4	1.4611	4.5167	3.8432	2.2135	2.13	1.43	1.09	0.76	-	-	-	-	-	-
LVS-002	4/17/2013	50.8	0.0996	4	1.4611	4.5167	3.9523	1.4164	1.6163	1.452	0.870	0.60	N	-	-	-	-	-
LVS-003	5/4/2013	50.8	0.1494	6	1.7895	4.5167	5.8282	2.2024	2.0434	1.764	1.084	0.61	N	-0.91	-0.74	0.17	0.024	0.019
LVS-004	5/4/2013	50.8	0.2491	10	2.3102	4.5167	9.7225	3.6149	2.9011	2.278	1.389	0.61	N	-1.18	-1.01	0.17	0.026	0.024
LVS-005	5/24/2013	50.8	0.3487	14	2.7335	4.5167	13.5405	4.0875	3.4302	2.688	1.602	0.60	N	-1.26	-1.23	0.03	0.022	0.023
LVS-006	6/24/2013	12.7	0.0579	2	1.1226	3.9437	2.0764	0.8161	1.2246	1.144	0.717	0.63	N	-0.26	-0.23	0.03	0.011	0.011
LVS-007	6/25/2013	12.7	0.1738	6	1.9443	3.9437	6.0654	0.0524	1.4584	1.955	0.574	0.29	Y	-2.57	-2.42	0.15	0.131	0.124
LVS-008	7/13/2013	12.7	0.1158	4	1.5875	3.9437	4.0784	0.5761	1.7040	1.603	0.603	0.38	Y	-1.86	-1.81	0.05	0.111	0.114
LVS-009	7/15/2013	76.2	0.1530	6	1.8124	4.4227	5.7286	1.8909	2.0914	1.771	1.017	0.57	N	-1.06	-0.97	0.09	0.023	0.023
LVS-010	7/21/2013	76.2	0.1020	4	1.4798	4.4227	3.8275	1.3589	1.6506	1.448	0.863	0.60	N	-0.29	-0.21	0.07	0.009	0.008
LVS-011	7/22/2013	76.2	0.1020	4	1.4798	4.4227	3.8532	1.3249	1.6584	1.452	0.852	0.59	N	-0.71	-0.74	-0.02	0.020	0.020
LVS-012	7/22/2013	76.2	0.1530	6	1.8124	4.4227	5.7663	1.9773	2.0672	1.777	1.040	0.59	N	-1.00	-1.01	-0.01	0.023	0.023
LVS-013	8/5/2013	76.2	0.1020	4	1.4798	4.4227	3.8122	1.3407	1.6881	1.445	0.857	0.59	N	-0.64	-0.57	0.07	0.018	0.016
LVS-014	8/5/2013	76.2	0.0510	2	1.0464	4.4227	1.9034	0.6262	1.1516	1.021	0.586	0.57	N	-0.21	-0.21	0.01	0.007	0.007
LVS-015	8/5/2013	76.2	0.0510	2	1.0464	4.4227	1.9106	0.6608	1.1422	1.023	0.602	0.59	N	-0.15	-0.17	-0.02	0.005	0.006
LVS-016	8/10/2013	50.8	0.0996	4	1.4611	4.5167	3.6999	1.3906	1.6026	1.405	0.862	0.61	N	-0.58	-0.55	0.03	0.017	0.017
LVS-017	8/10/2013	50.8	0.1494	6	1.7895	4.5167	5.5357	2.0818	2.0736	1.719	1.054	0.61	N	-0.85	-0.82	0.03	0.022	0.021
LVS-018	8/12/2013	50.8	0.0498	2	1.0332	4.5167	1.9709	0.8116	1.1151	1.026	0.658	0.64	N	-0.12	-0.04	0.08	0.002	0.002
LVS-019	8/12/2013	50.8	0.0498	2	1.0332	4.5167	1.9859	0.8186	1.1091	1.030	0.661	0.64	N	-0.12	-0.12	0.00	0.005	0.004
LVS-020	8/17/2013	25.4	0.1530	6	1.8124	4.7167	6.0210	2.5021	2.1651	1.747	1.126	0.64	N	-0.88	-0.89	-0.01	0.024	0.023
LVS-021	8/18/2013	25.4	0.1530	6	1.8124	4.7167	6.0797	2.3841	2.0589	1.755	1.099	0.63	N	-0.91	-0.91	0.00	0.023	0.023
LVS-022	8/18/2013	25.4	0.1020	4	1.4798	4.7167	4.0270	1.6609	1.6266	1.428	0.917	0.64	N	-0.58	-0.60	-0.02	0.018	0.019
LVS-023	8/18/2013	25.4	0.0510	2	1.0464	4.7167	1.9866	0.8421	1.1040	1.003	0.653	0.65	N	-0.16	-0.13	0.03	0.007	0.006
LVS-024	8/18/2013	25.4	0.0510	2	1.0464	4.7167	1.9903	0.8043	1.0902	1.004	0.638	0.64	N	-0.20	-0.20	0.00	0.008	0.009
LVS-025	8/19/2013	25.4	0.1020	4	1.4798	4.7167	4.0006	1.6290	1.6407	1.424	0.909	0.64	N	-0.32	-0.29	0.03	0.009	0.009
LVS-026	9/2/2013	25.4	0.1020	4	1.4798	4.7167	4.0807	1.6996	1.7070	1.438	0.928	0.65	N	-0.62	-0.64	-0.01	0.018	0.019
LVS-027	9/2/2013	50.8	0.0996	4	1.4611	4.5167	3.7979	1.4799	1.6314	1.424	0.889	0.62	N	-0.62	-0.60	0.02	0.018	0.019
LVS-028	9/2/2013	50.8	0.1494	6	1.7895	4.5167	5.7530	2.1526	2.0256	1.752	1.072	0.61	N	-1.07	-0.97	0.10	0.026	0.023
LVS-029	9/19/2013	12.7	0.1158	4	1.5875	3.9437	4.0483	0.4968	-	1.597	0.560	0.35	Y	-1.65	-1.49	0.16	0.084	0.082
LVS-030	9/19/2013	12.7	0.0579	2	1.1226	3.9437	2.0852	0.8415	1.1811	1.146	0.728	0.64	N	-0.12	-0.12	0.00	0.005	0.006
LVS-031	12/9/2013	25.4	0.2375	10	2.2509	4.7167	9.4116	3.6469	2.6902	2.184	1.359	0.62	N	-1.27	-1.26	0.01	0.027	0.027
LVS-032	12/9/2013	25.4	0.3325	14	2.6634	4.7167	13.2250	0.9833	3.1496	2.589	0.706	0.27	Y	-3.29	-3.10	0.19	0.108	0.104
LVS-033	12/9/2013	76.2	0.3569	14	2.7685	4.4227	12.7223	4.3935	3.3374	2.639	1.551	0.59	N	-1.64	-1.58	0.06	0.028	0.027

Notes:

LVS-001 Test malfunction - Site impacted twice with 4 J
LVS-002 Immediate and relaxed dent information not available
LVS-007 Cracking in center of top face sheet and at tip boundary
LVS-008 Cracking in center of top face sheet
LVS-029 Force data clipped at 0.9199 kN
LVS-032 Cracking in center of top face sheet

APPENDIX II. FORCE AND DENT PROFILES

The force versus time history plots are included here for each impact. Both immediate and relaxed dent profiles are included next to its corresponding force plot. These plots are organized by impact tip radius and increasing measured kinetic energy to better compare similar tests. Force data for LVS-029 was clipped and not included. Detailed data on maximum force and dent depths can be found in Appendix I. Dent profile for test LVS-002 is not available.

Appendix IIa. R12.7 mm

LVS-006, 2.08 J

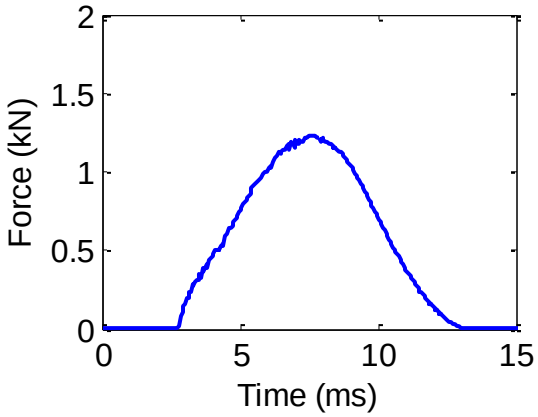

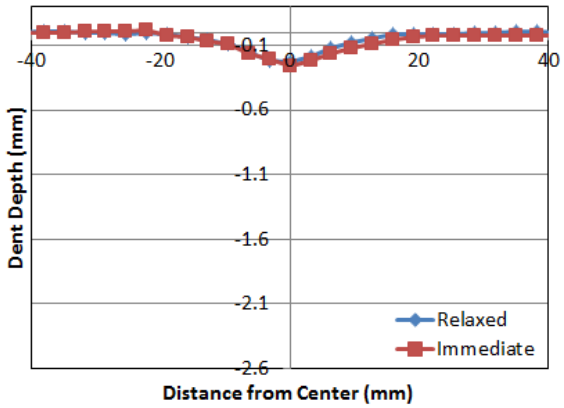

LVS-030, 2.09 J

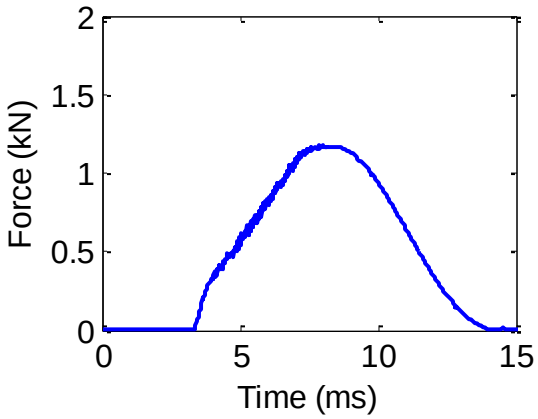

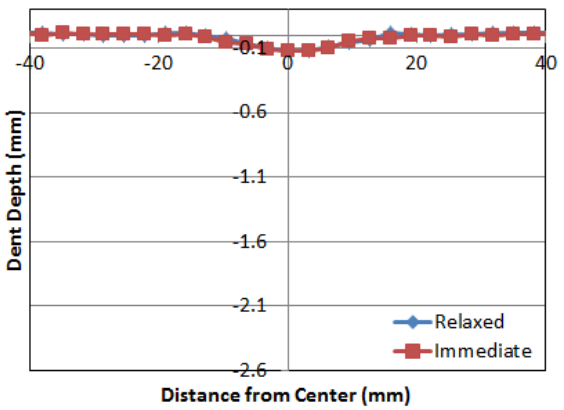

LVS-029, 4.05 J (Force data clipped)

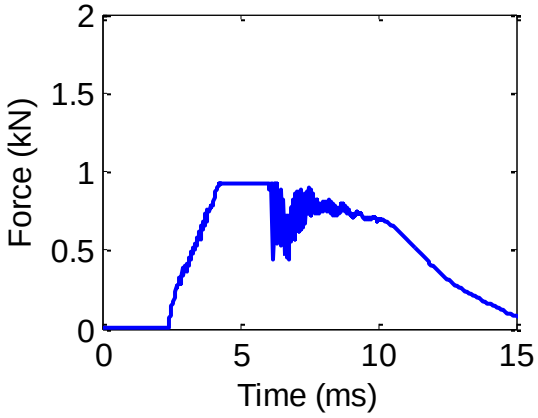

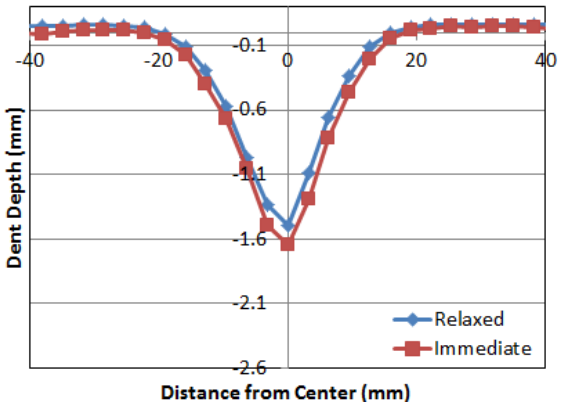

LVS-008, 4.08 J

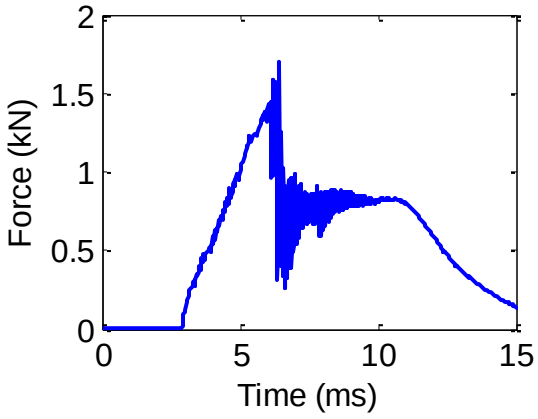

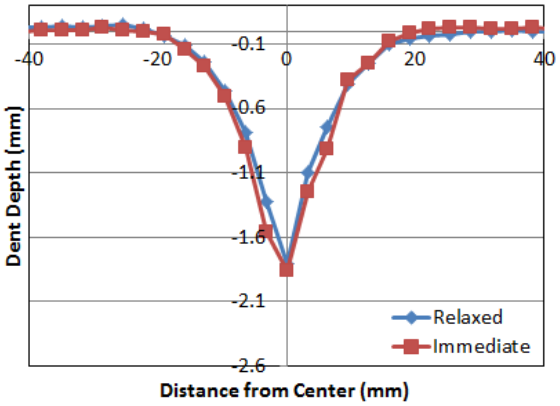

LVS-007, 6.07 J

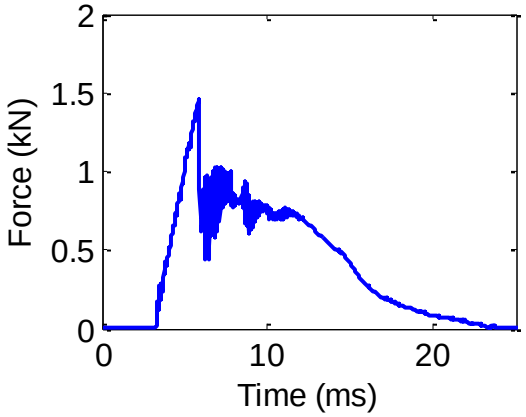

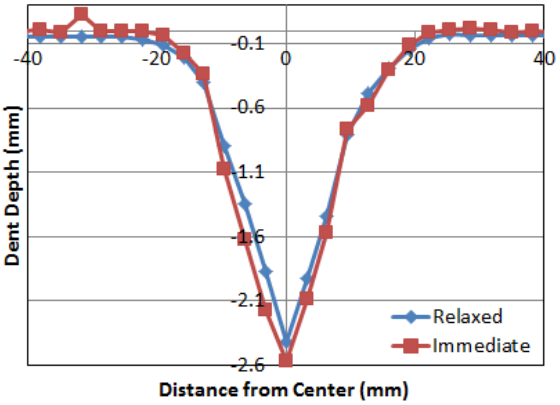

Appendix IIb. R25.4 mm

LVS-023, 1.99 J

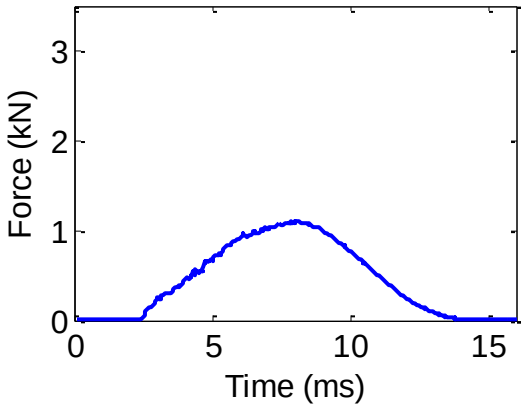

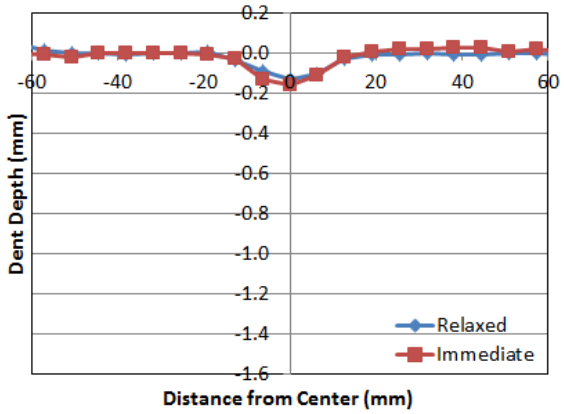

LVS-024, 1.99 J

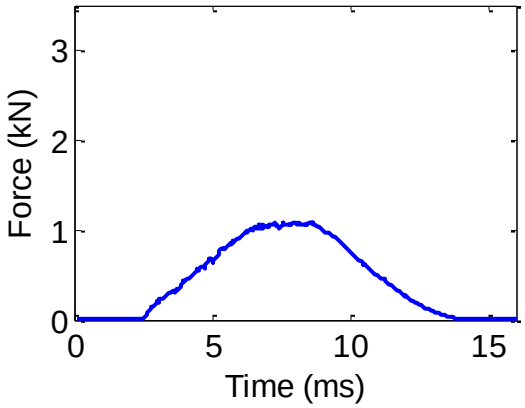

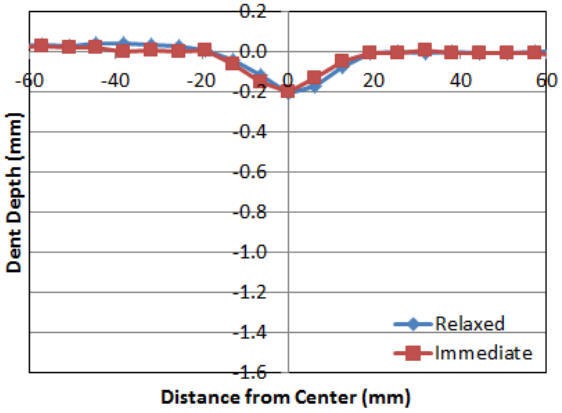

LVS-025, 4.00 J

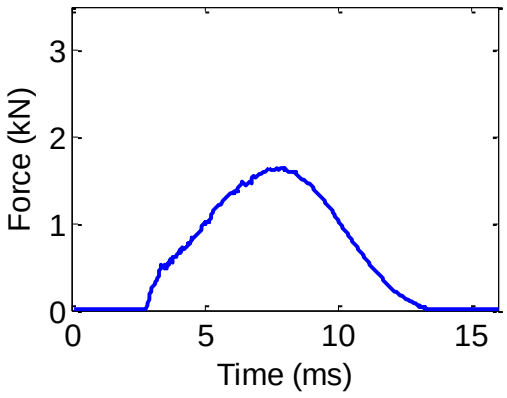

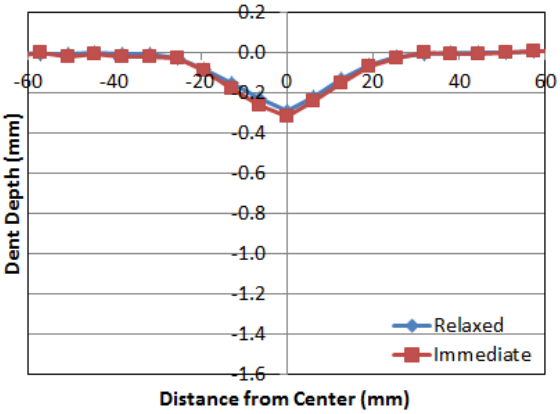

LVS-022, 4.03 J

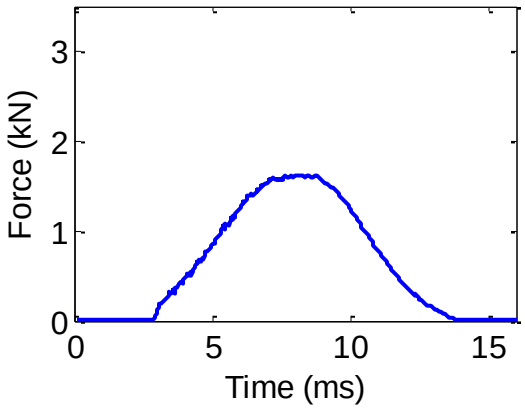

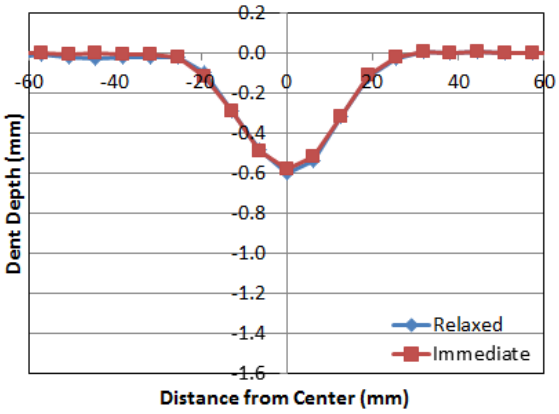

LVS-026, 4.08 J

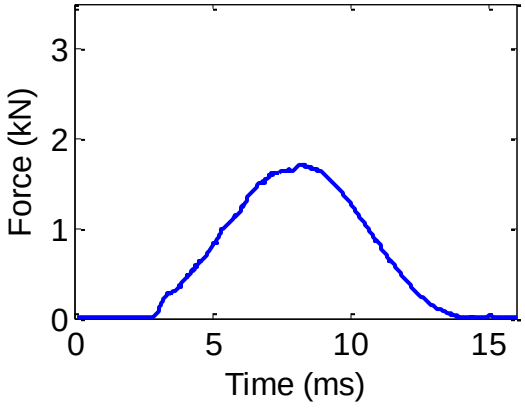

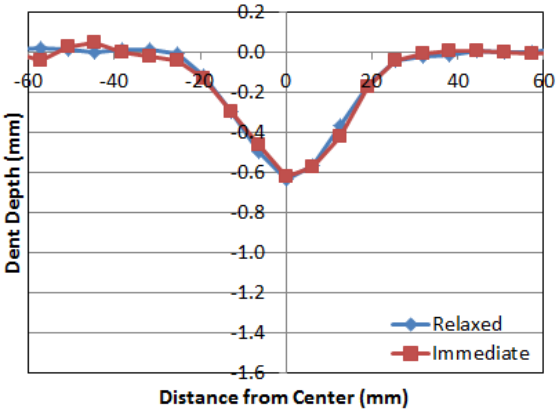

LVS-020, 6.02 J

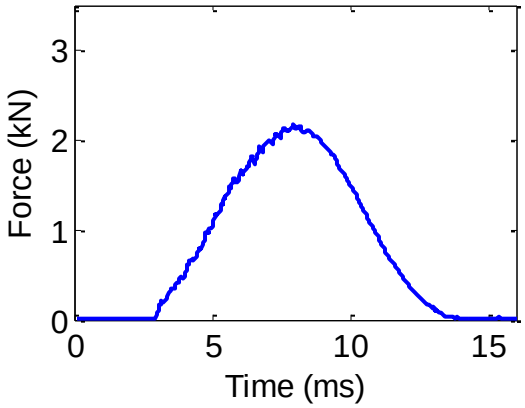

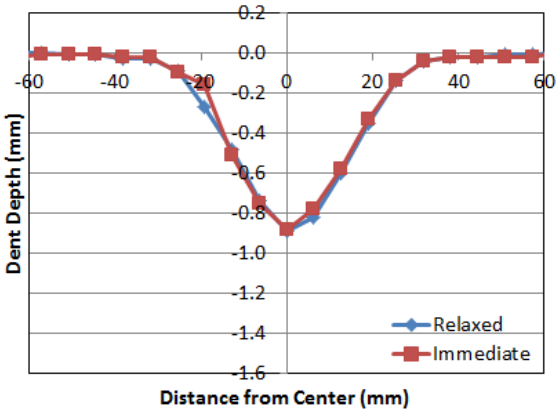

LVS-021, 6.08 J

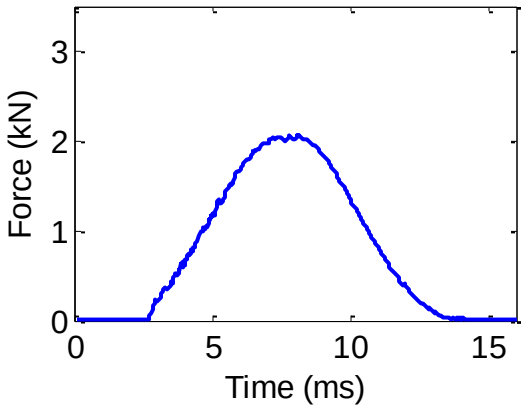

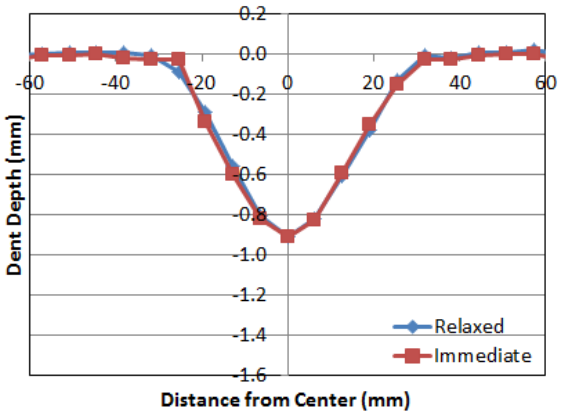

LVS-031, 9.41 J

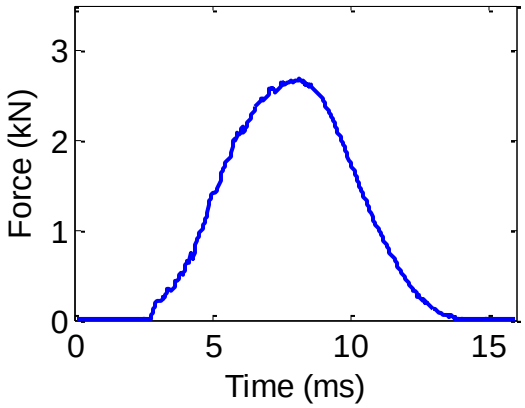

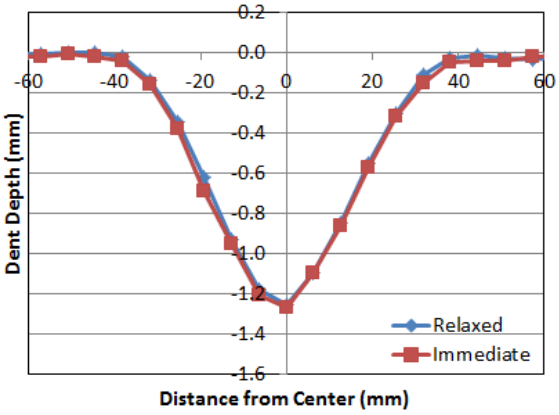

LVS-032, 13.23 J (Cracking in facesheet)

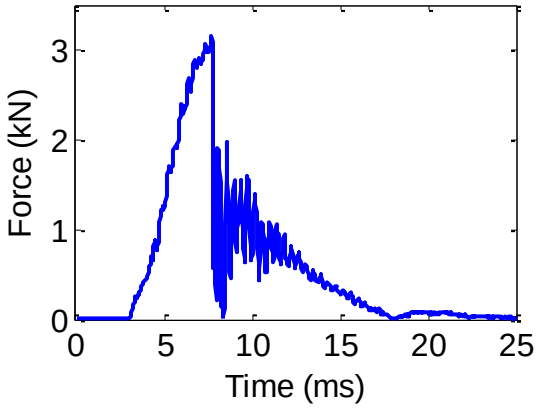

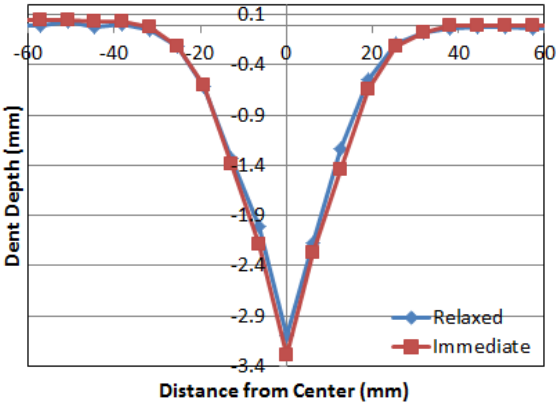

Appendix IIc. R50.8 mm

LVS-018, 1.97 J

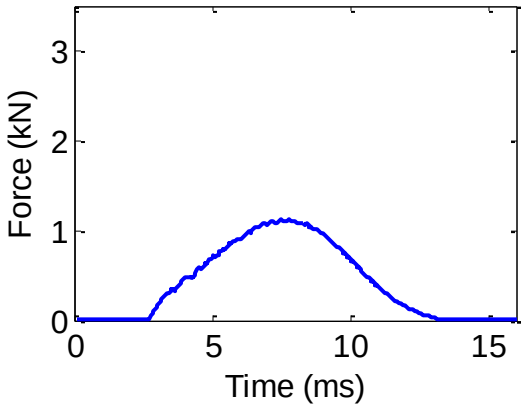

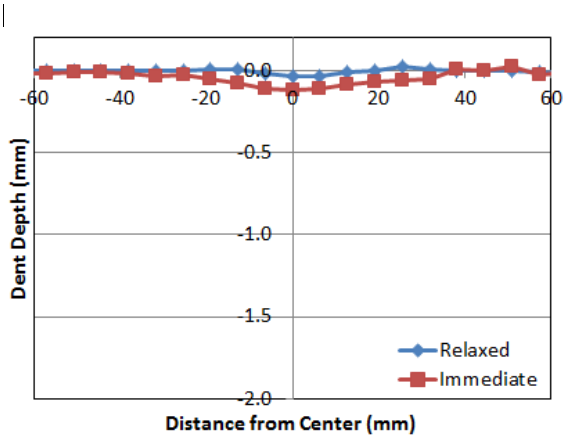

LVS-019, 1.99 J

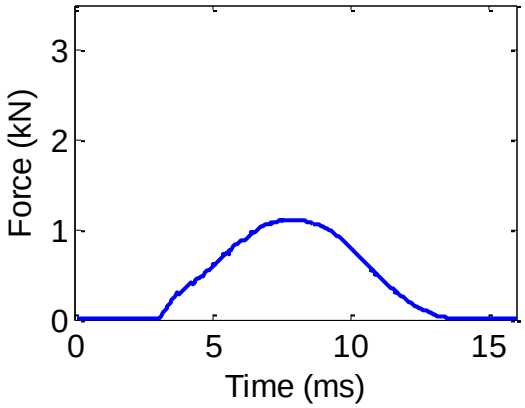

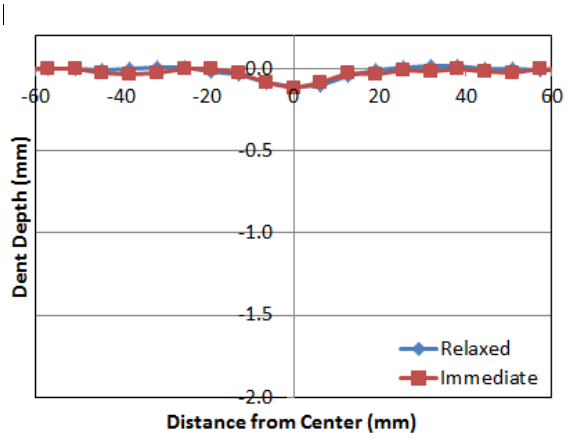

LVS-016, 3.70 J

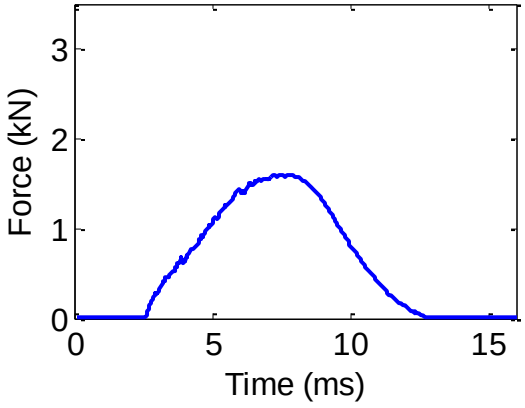

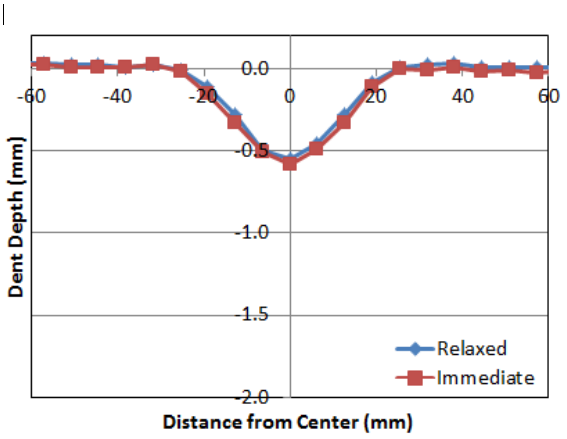

LVS-027, 3.80 J

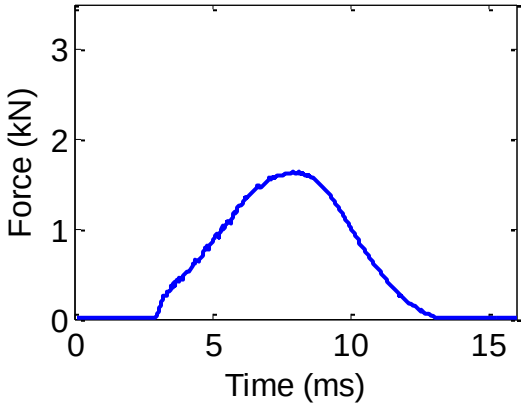

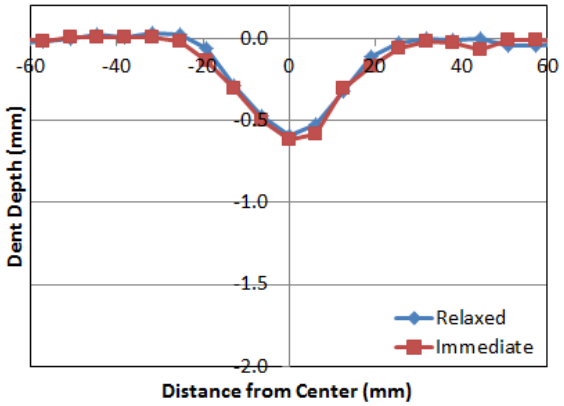

LVS-002, 3.95 J (Dent information not available)

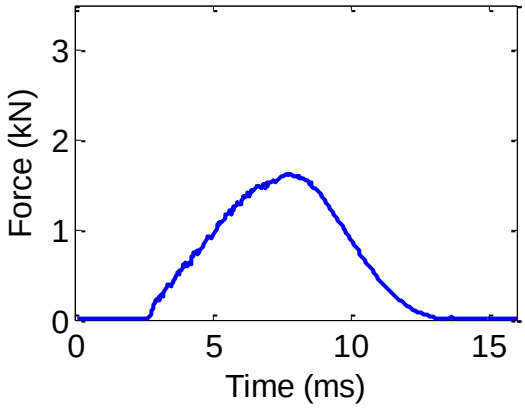

LVS-017, 5.54 J

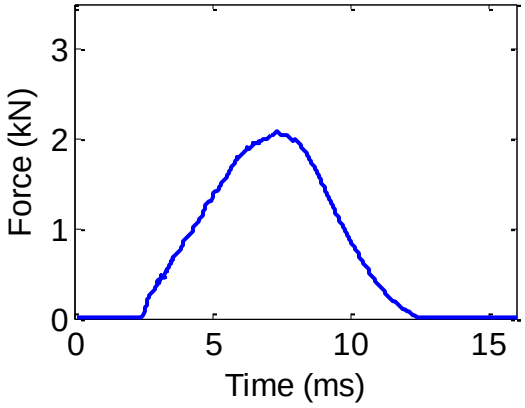

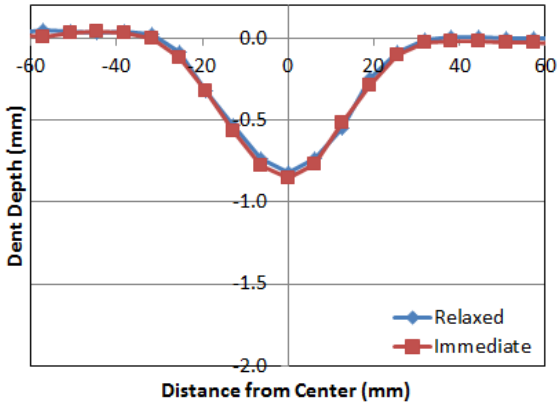

LVS-028, 5.75 J

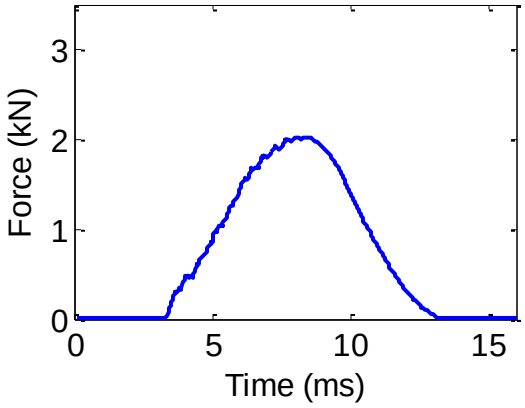

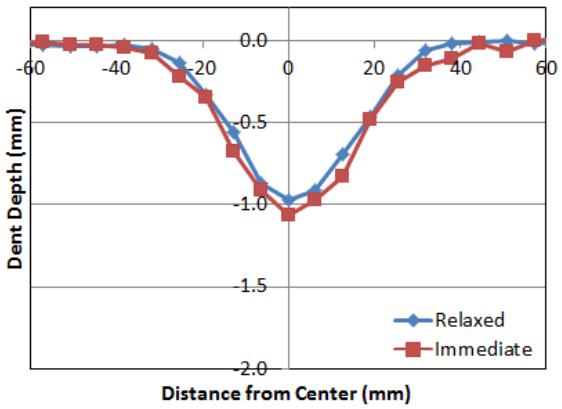

LVS-003, 5.83 J

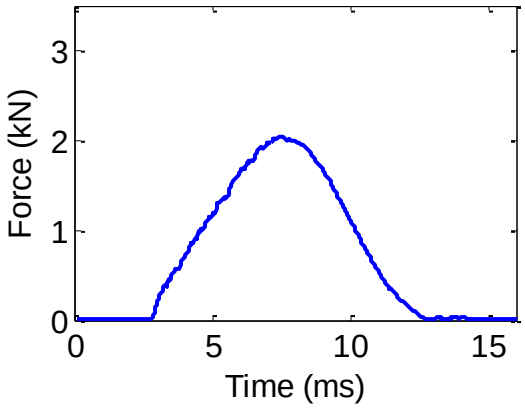

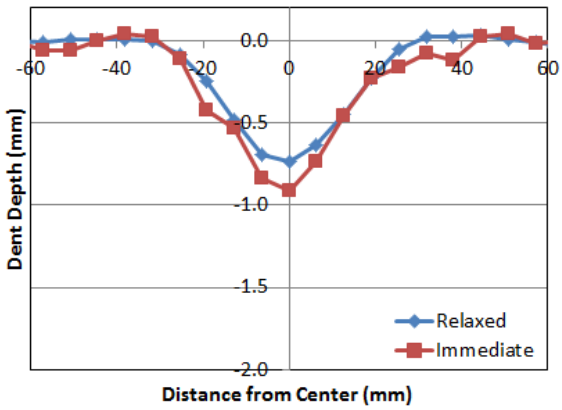

LVS-004, 9.72 J

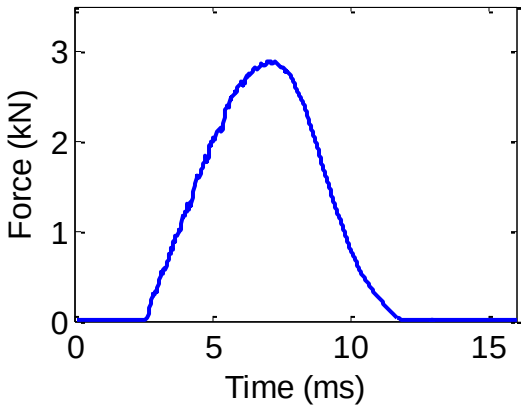

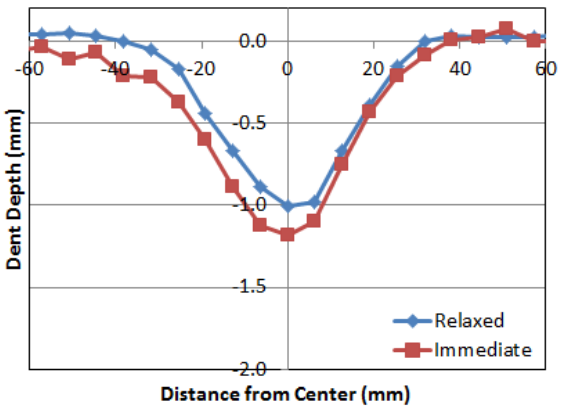

LVS-005, 13.54 J

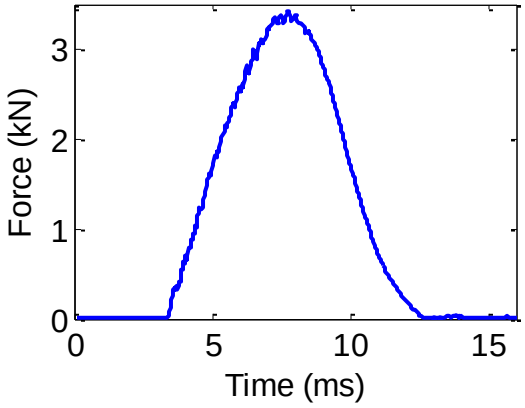

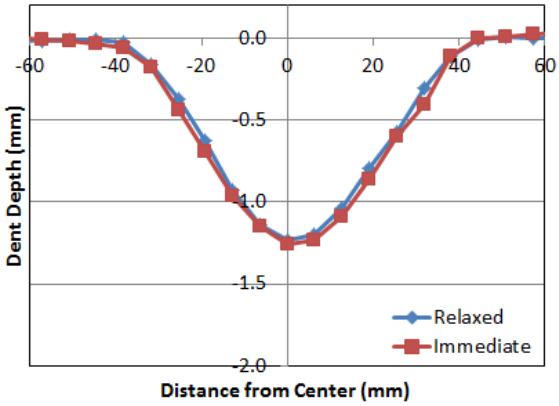

Appendix IIId. R76.2 mm

LVS-014, 1.90 J

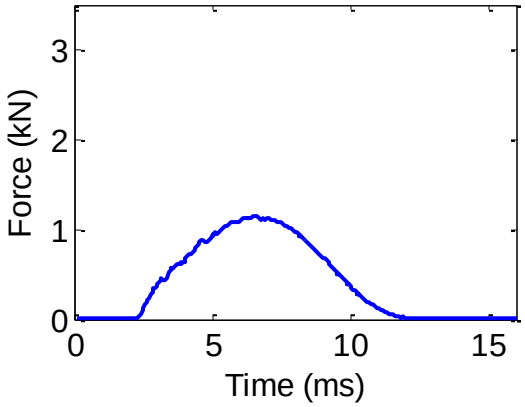

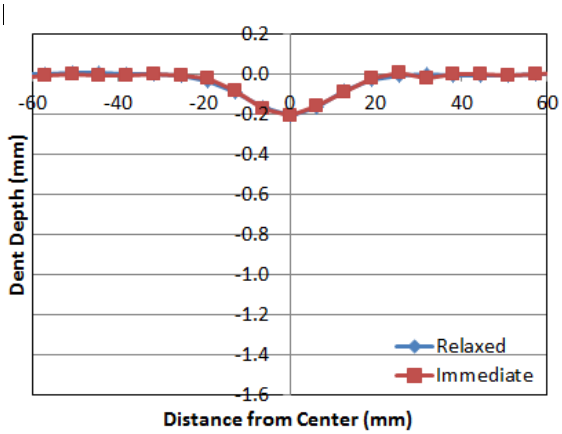

LVS-015, 1.91 J

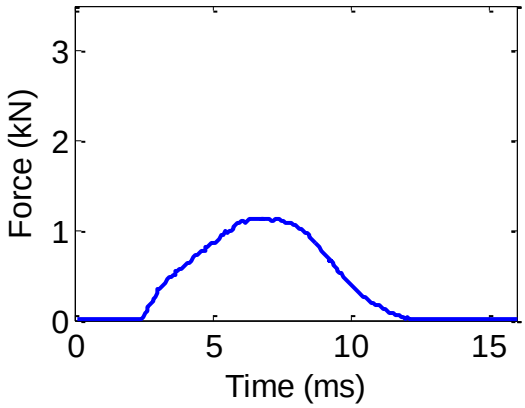

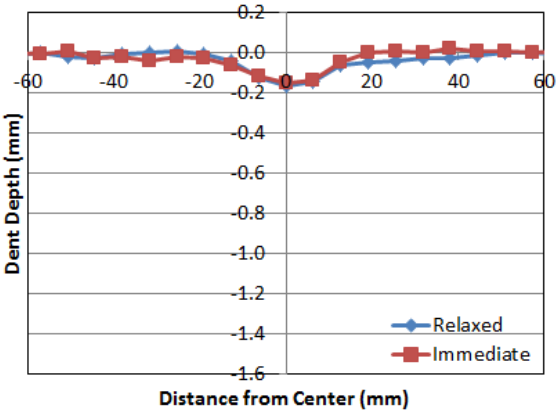

LVS-013, 3.81 J

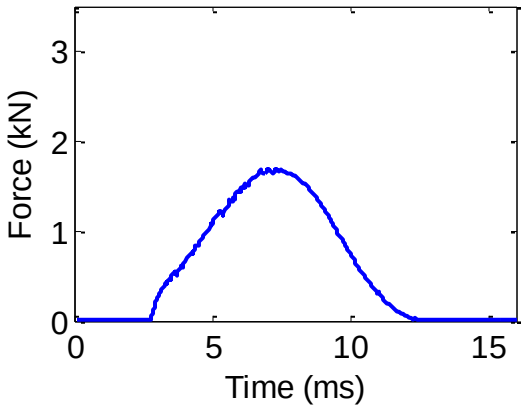

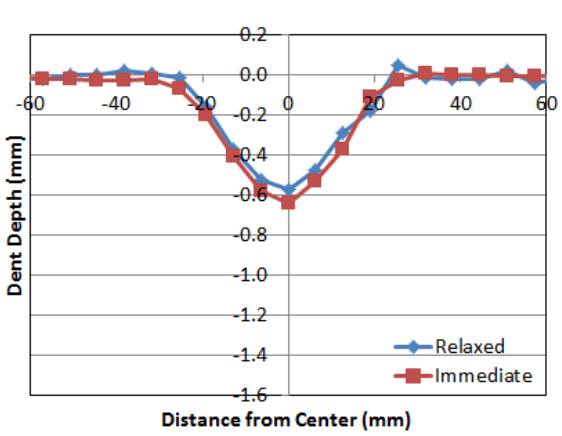

LVS-010, 3.83 J

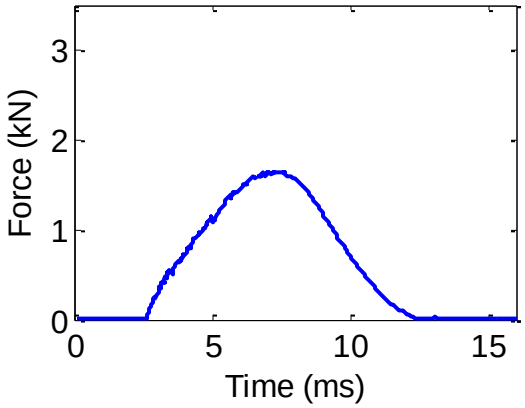

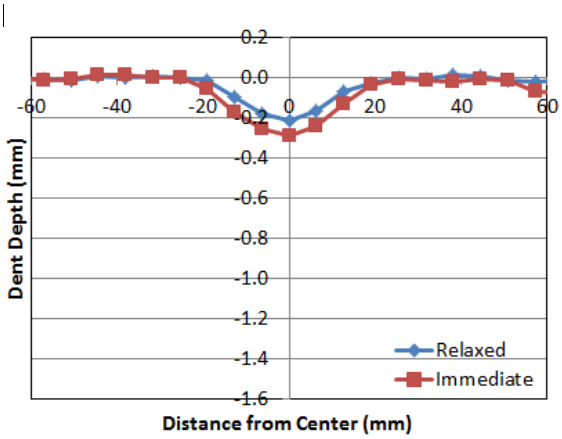

LVS-011, 3.85 J

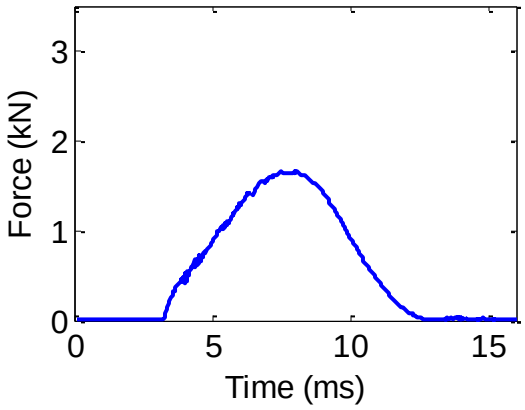

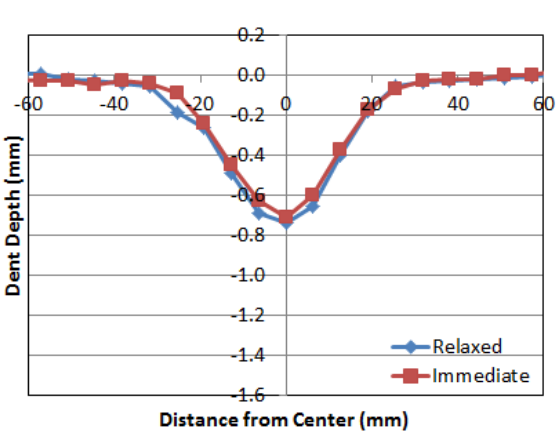

LVS-009, 5.73 J

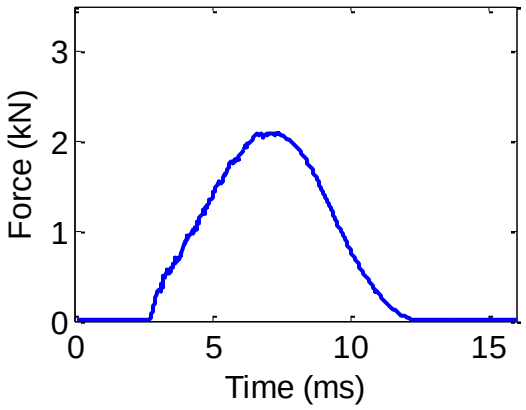

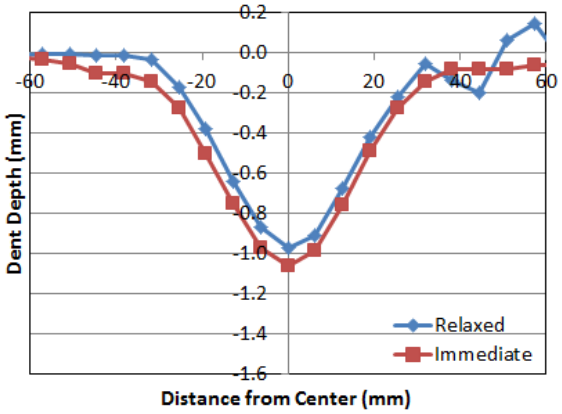

LVS-012, 5.77 J

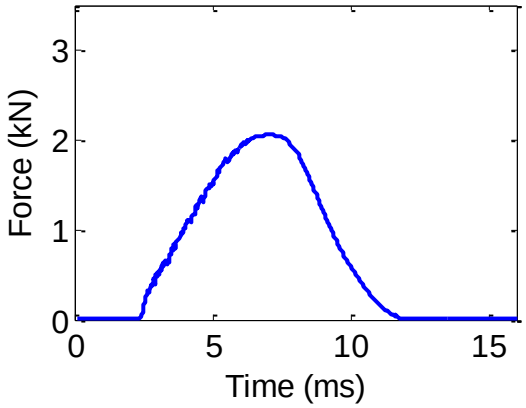

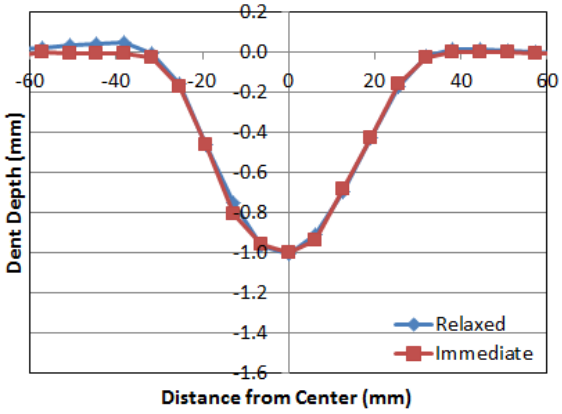

LVS-033, 12.72 J

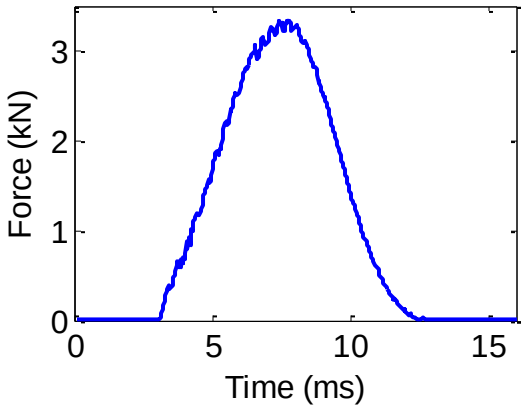

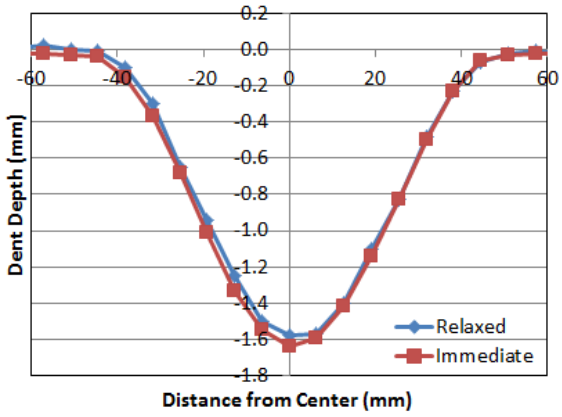

APPENDIX III. INTERNAL CORE DAMAGE

Appendix IIIa. Damage Progression by Tip Radius

Impact Tip R12.7 mm

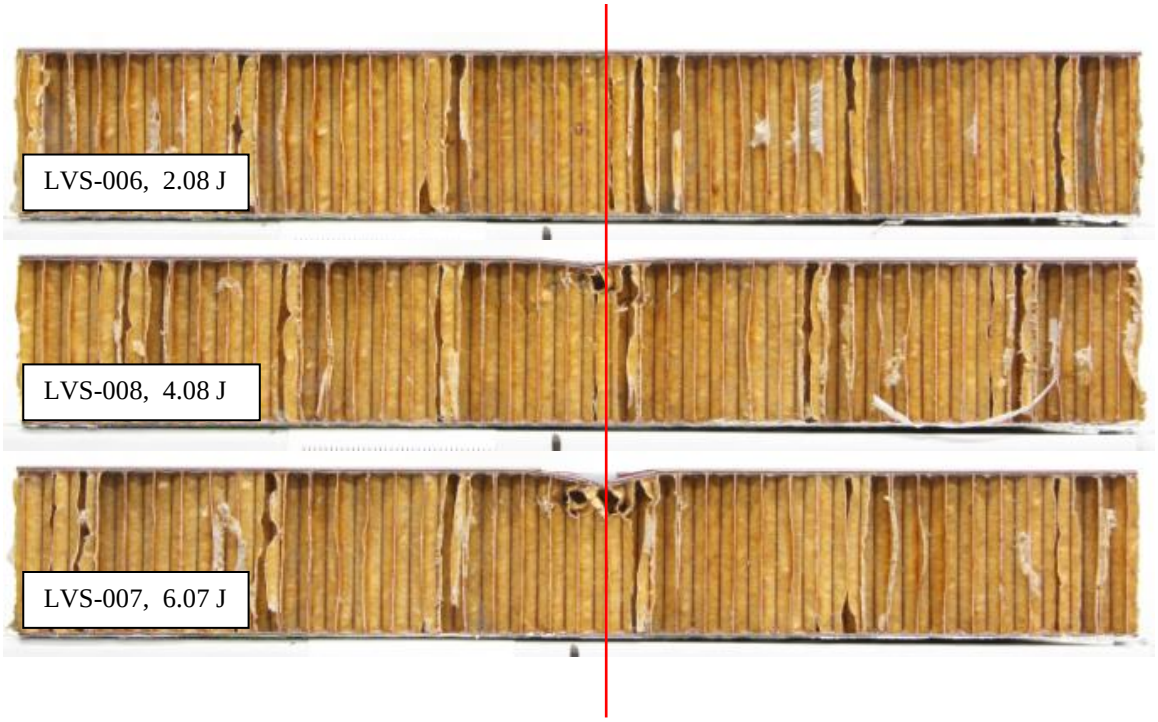

Impact Tip R25.4 mm

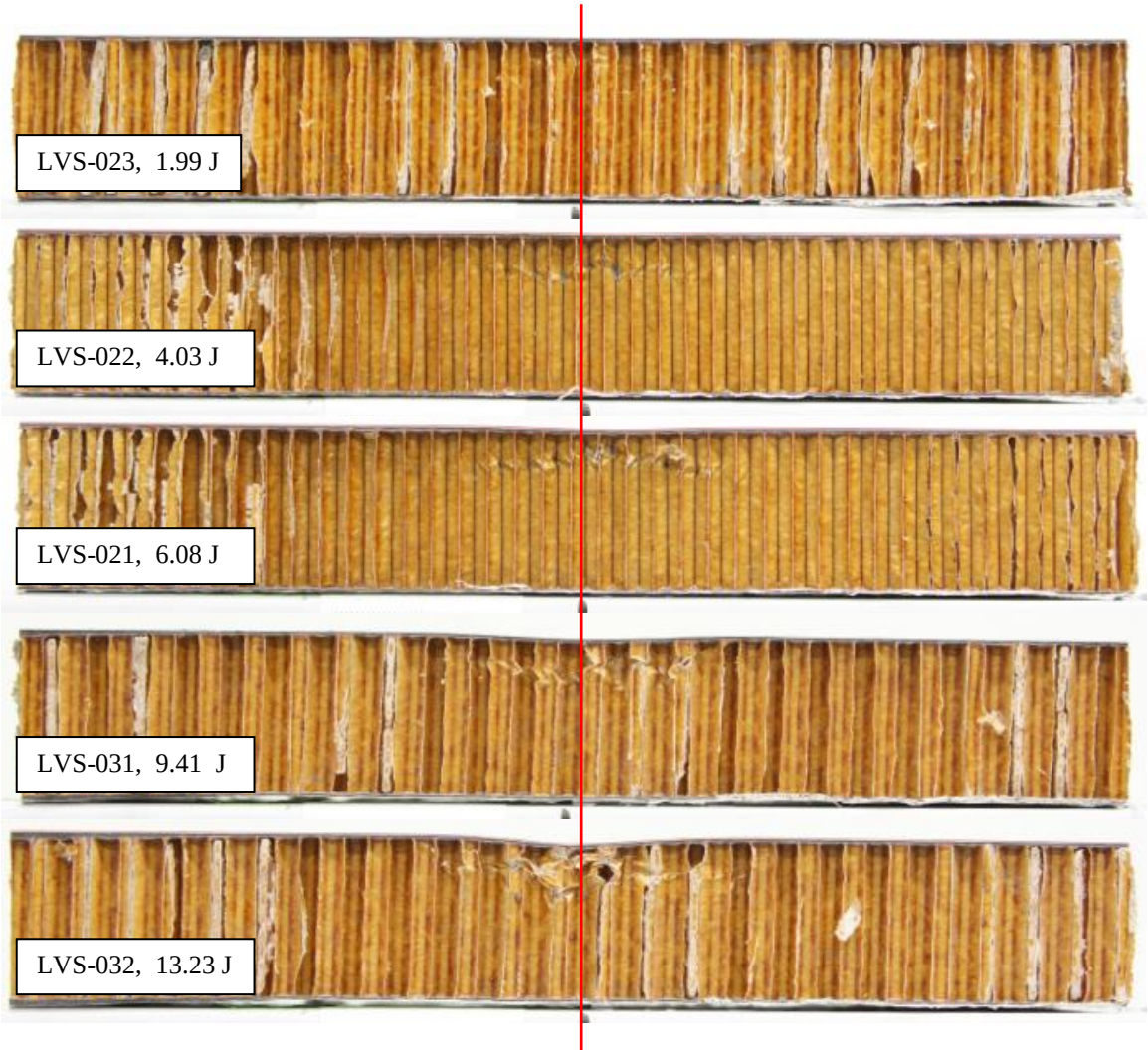

Impact Tip R50.8 mm

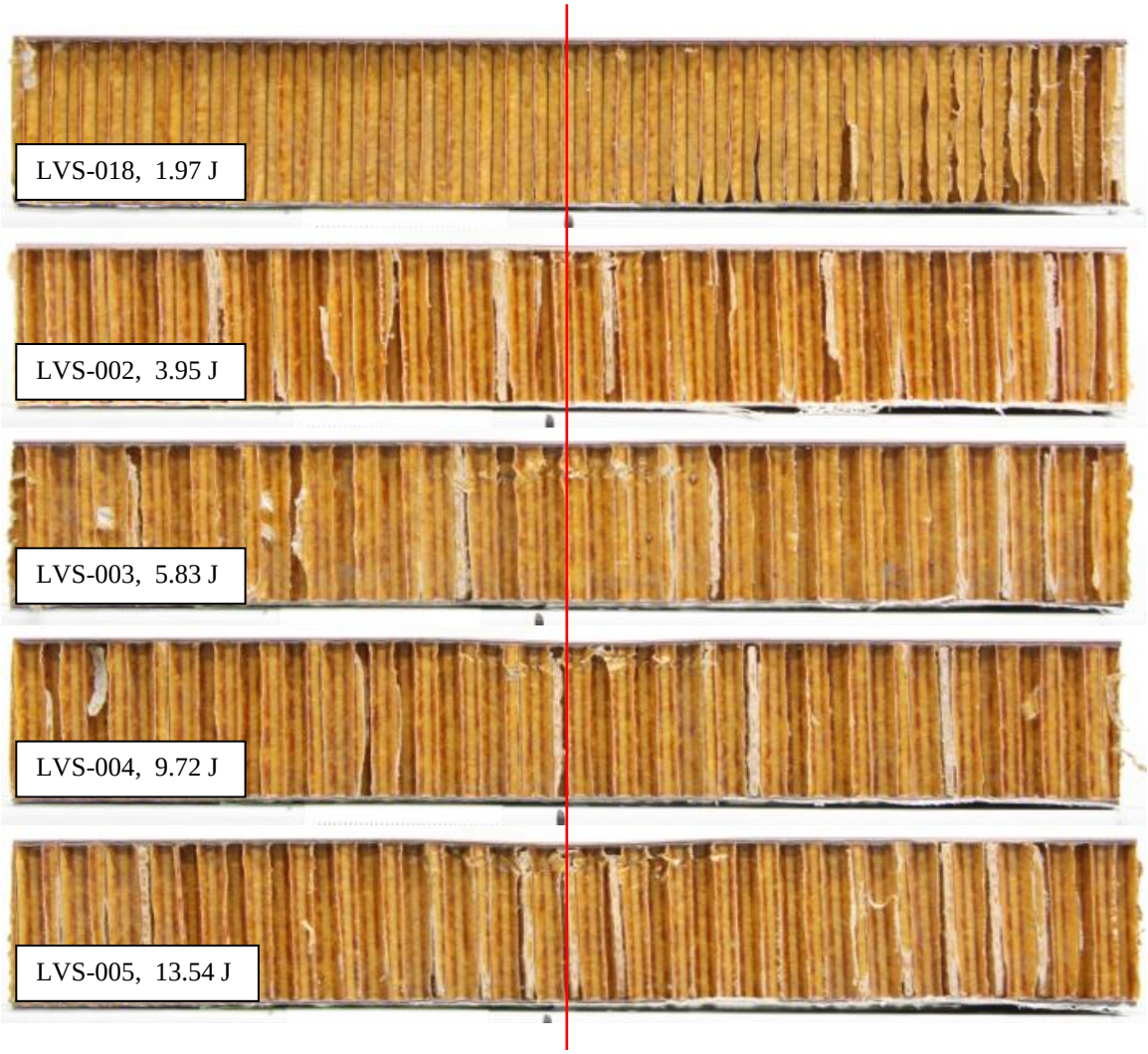

Impact Tip R76.2 mm

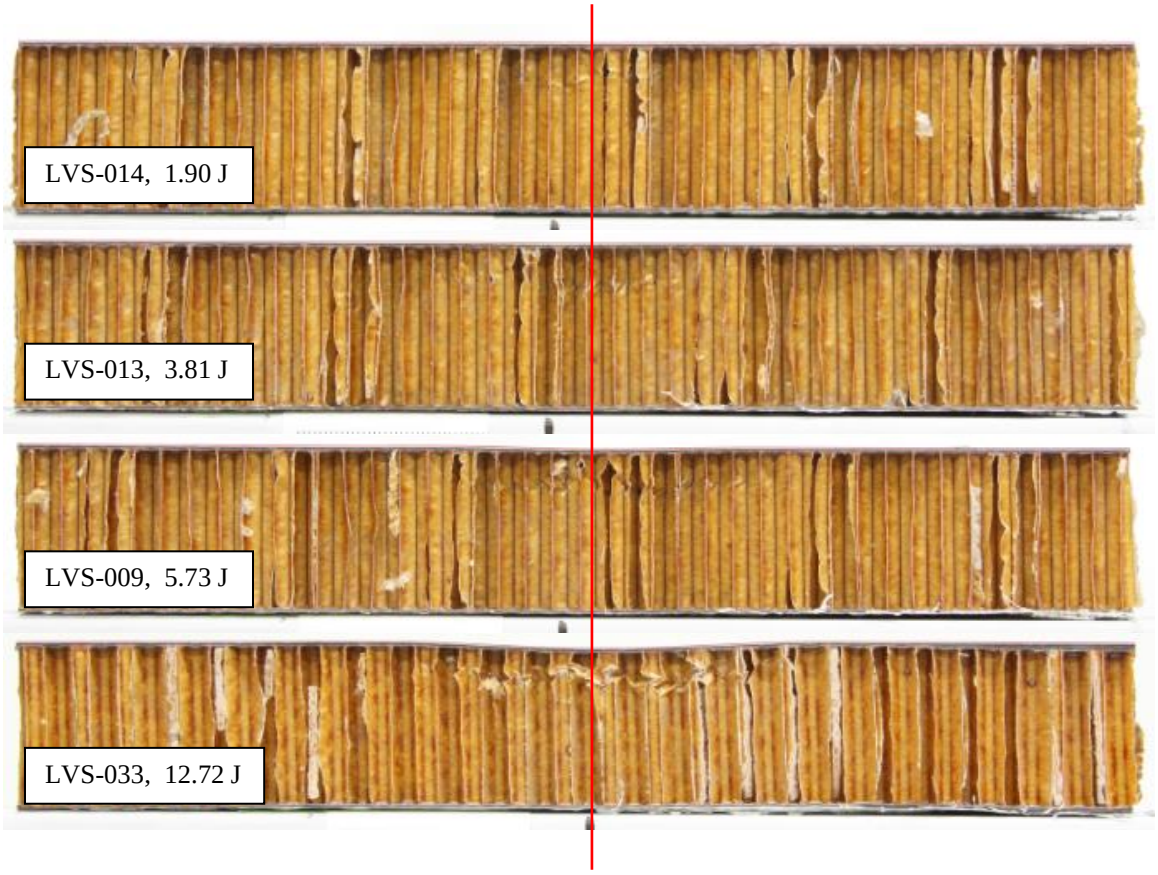

Appendix IIIb. Internal Core Damage

Images of internal core for test sites cut through center of impact are included. The left side of the cut is shown followed by the right side. The scale is the same for all images and is included in the first one for reference.

LVS-001, R50.8, 3.84 J

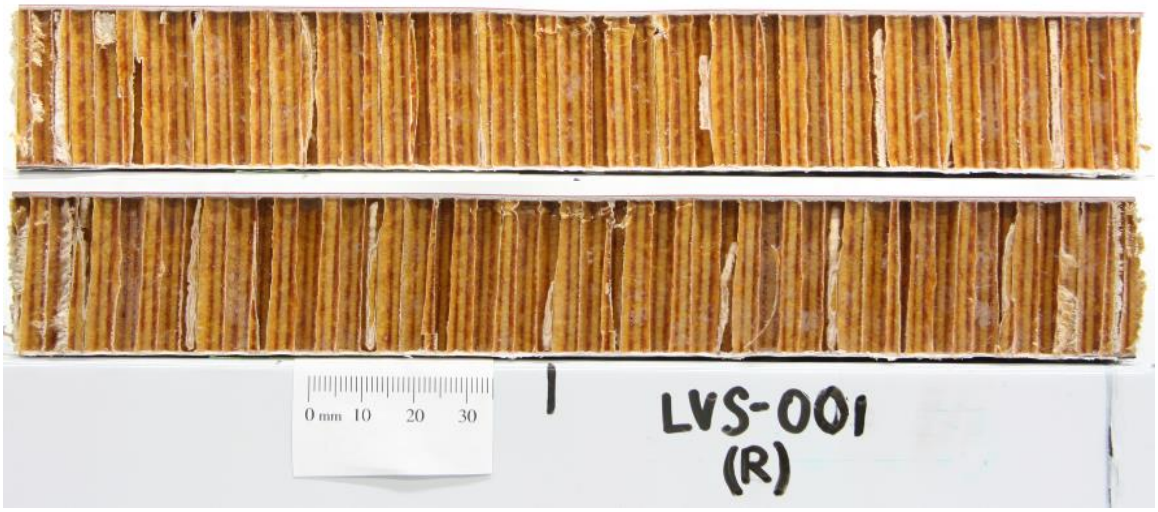

LVS-002, R50.8, 3.95 J

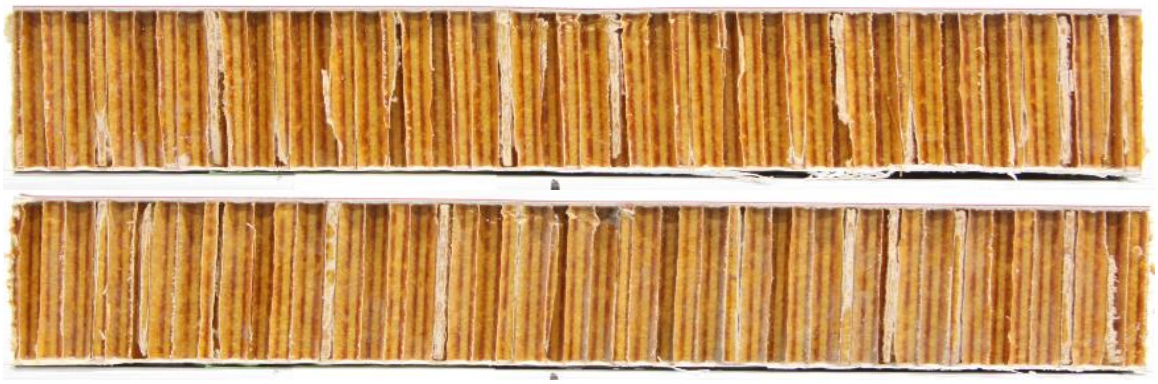

LVS-003, R50.8, 5.83J

LVS-004, R50.8, 9.72 J

LVS-005, R50.8, 13.54 J

LVS-006, R12.7, 2.08 J

LVS-007, R12.7, 6.07 J

LVS-008, R12.7, 4.08 J

LVS-009, R76.2, 5.73 J

LVS-010, R76.2, 3.83 J

LVS-011, R76.2, 3.85 J

LVS-012, R76.2, 5.77 J

LVS-013, R76.2, 3.81 J

LVS-014, R76.2, 1.90 J

LVS-015, R76.2, 1.91 J

LVS-016, R50.8, 3.70 J

LVS-017, R50.8, 5.54 J

LVS-018, R50.8, 1.97 J

LVS-019, R50.8, 1.99 J

LVS-020, R25.4, 6.02 J

LVS-021, R25.4, 6.08 J

LVS-022, R25.4, 4.03 J

LVS-023, R25.4, 1.99 J

LVS-024, R25.4, 1.99 J

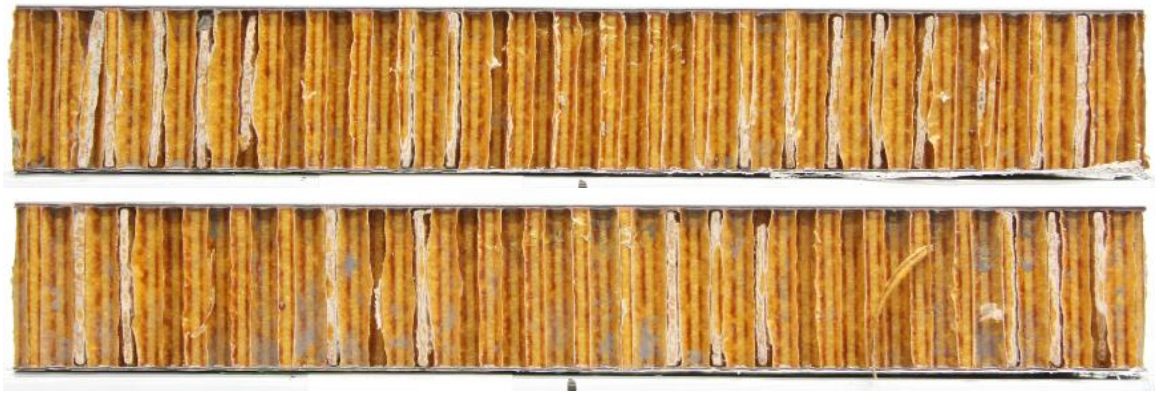

LVS-025, R25.4, 4.00 J

LVS-026, R25.4, 4.0807 J

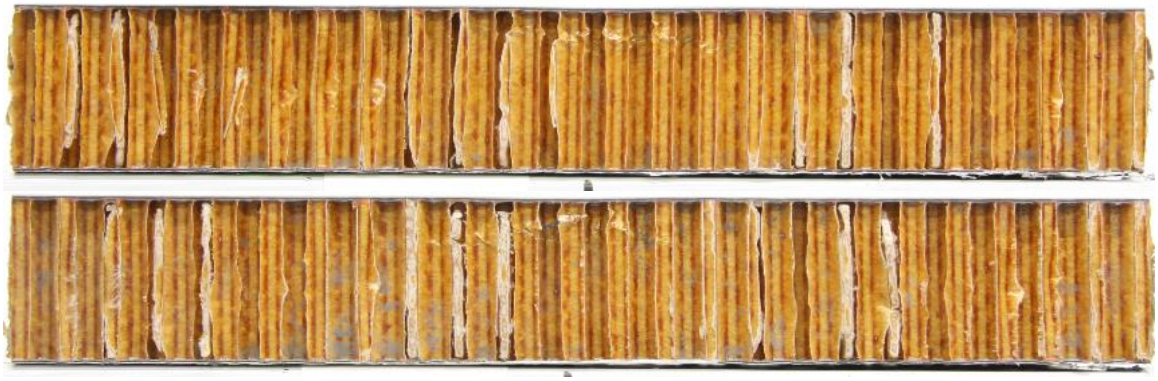

LVS-027, R50.8, 3.80 J

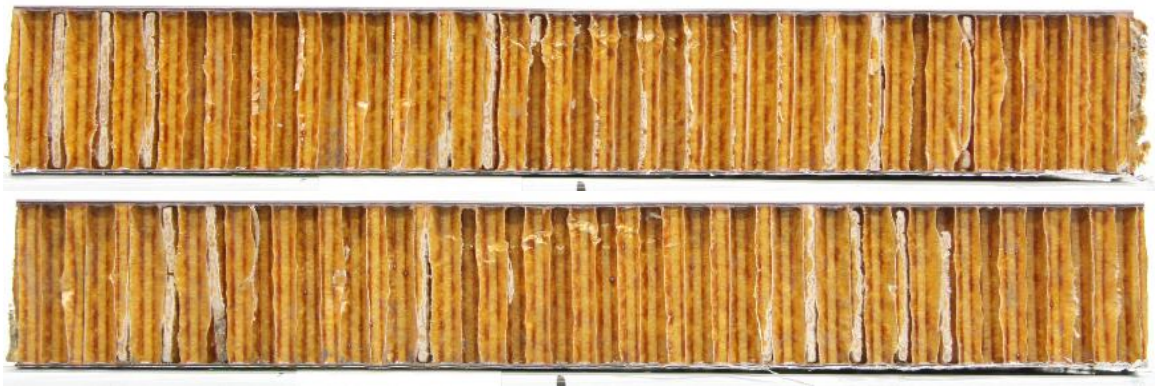

LVS-028, R50.8, 5.75 J

LVS-029, R12.7, 4.05 J

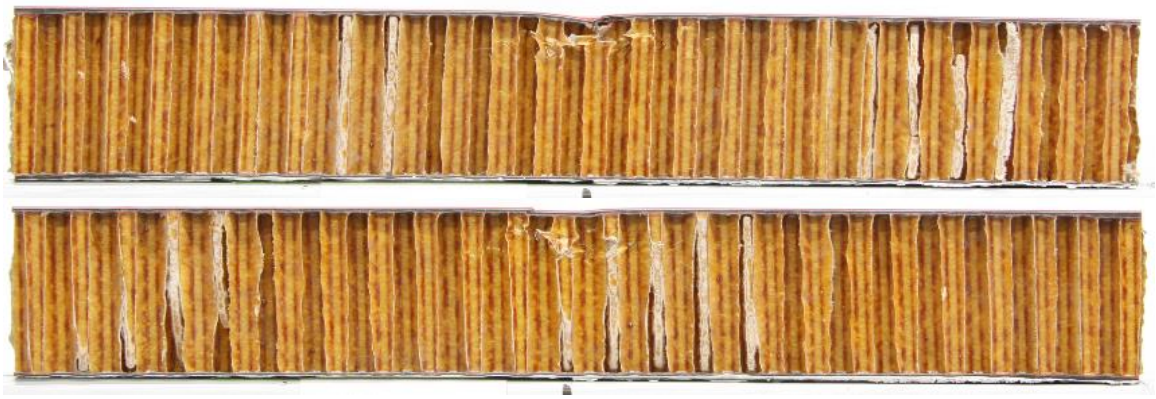

LVS-030, R12.7, 2.09 J

LVS-031, R25.4, 9.41 J

LVS-032, R25.4, 13.23 J

LVS-033, R76.2, 12.72 J

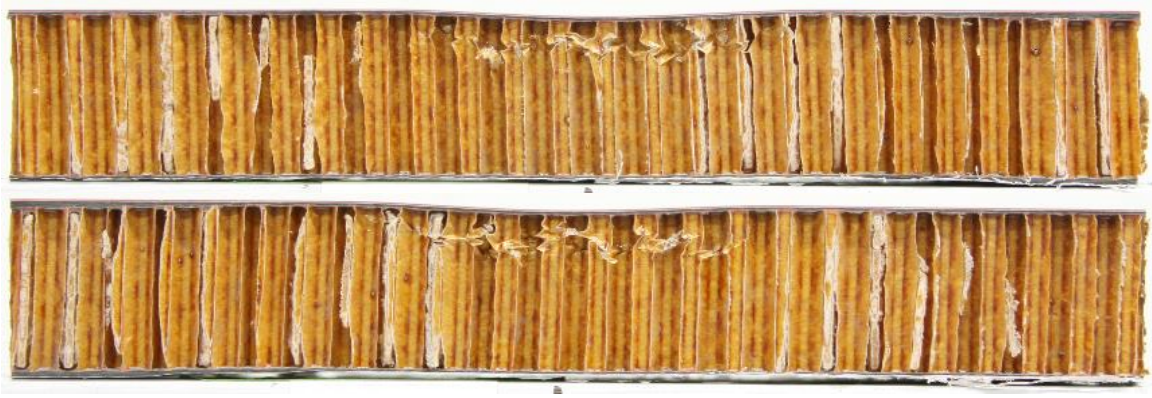

APPENDIX IV. POTENTIAL ENERGY CALCULATIONS AND DATA EXTRACTION

An energy balance model was used in order to calculate the height of the pendulum required for a desired potential energy. The height and pendulum arm position are determined using a modified version of Delaney's MATLAB code [17] and is included below.

```
function Potential_Energy2_ReducedMass
%%% Additional masses 3, 4, 5 (377.9g 378.6g and 377.8g) removed

%%% -- ENTER TEST DATA --
STEP=input('Initial STEP = ');
PE=input('Potential Energy = ');
tip=input('Tip Radius = ');
if tip==50.8
    MASS=(4.813+(-377.9-378.6-377.8)/1000); %R50.8mm
elseif tip==152.4
    MASS=(4.849+(-377.9-378.6-377.8)/1000); %R152.4mm
elseif tip==101.6
    MASS=(4.841+(-377.9-378.6-377.8)/1000);  %R101.6mm
elseif tip==12.7
    MASS=(4.240+(-377.9-378.6-377.8)/1000); %R12.7mm
elseif tip==25.4
    MASS=(5.013+(-377.9-378.6-377.8)/1000); %R=25.4mm
elseif tip==76.2
    MASS=4.719-(.3786+.3778+.3779); %R=76.2mm
else
    MASS=input('Pendulum Mass = ');
end
%%% -- CONSTANT DATA --
MBAR=0.838;%Mass of the fiberglass bar
L=1.4224;%dist from pivot to mass CG
G=9.80665;

%%% -- CALCULATIONS --
LB=0.70485; %dist. from pivot to bar CG
THETA=acosd(1-PE/(G*(MBAR*LB+MASS*L)));

VEL=L*sqrt((G*(1-
cosd(THETA))*(MBAR*LB+MASS*L))/(((1/6)*MBAR*LB^2)+(0.5*MASS*L^2)));
KE=(1/6)*MBAR*LB^2*(VEL/L)^2+0.5*MASS*VEL^2;

HGT=STEP-(10*THETA);
LOW_H=ceil(HGT);%LOW ENERGY HEIGHT
LOW_T=(STEP-LOW_H)/10;
LOW_STEP=STEP-(10*LOW_T);
```

```
LOW_V=L*sqrt((G*(1-
cosd(LOW_T))*(MBAR*LB+MASS*L))/(((1/6)*MBAR*LB^2)+(0.5*MASS*L^2)));
LOW_E=(1/6)*MBAR*LB^2*(LOW_V/L)^2+0.5*MASS*LOW_V^2;

HI_H=floor(HGT);%HIGH ENERGY HEIGHT
HI_T=(STEP-HI_H)/10;
HI_STEP=STEP-(10*HI_T);
HI_V=L*sqrt((G*(1-
cosd(HI_T))*(MBAR*LB+MASS*L))/(((1/6)*MBAR*LB^2)+(0.5*MASS*L^2)));
HI_E=(1/6)*MBAR*LB^2*(HI_V/L)^2+0.5*MASS*HI_V^2;

HEIGHT=L*(1-cosd(THETA));

fprintf('\nENERGY= %4.4fJ  vel= %4.4fm/s\n',PE,VEL)
fprintf('STEP= %4.4g for high energy of %4.4fJ\n',HI_STEP,HI_E)
fprintf('STEP= %4.4g for low  energy of %4.4fJ\n',LOW_STEP,LOW_E)
fprintf('HEIGHT= %4.4f m\n\n',HEIGHT)

TOT_MASS=MASS+MBAR
```

Peak force, inbound velocity, and kinetic energy information was extracted from the raw data using the following MATLAB code.

```
function Datacrunch
%% LOAD TEST DATA
tip=input('Tip Radius: ');
fprintf('Test ID:')
dat1=input('');
dat2=[dat1 '.txt'];
[t1,z,l]=SingleAnalysis_ALL(dat2);
t=t1*10^-9;% t1 input as nanoseconds, t outputs seconds
if tip==50.8
    MASS=4.813-(.3786+.3778+.3779); %R50.8mm
    F1=z*1000*20.786*1.092;
elseif tip==152.4
    MASS=4.849-(.3786+.3778+.3779); %R152.4mm
    F1=z*1000*20.786*1.099;
    %sensor=1 mv for every 20.8N
elseif tip==101.6
    MASS=4.841-(.3786+.3778+.3779);  %R101.6mm
    F1=z*1000*20.786*1.097;
elseif tip==12.7
    MASS=4.240-(.3786+.3778+.3779); %R12.7mm
    F1=(z*1000)*4.5858*1.006;
elseif tip==25.4
    MASS=5.013-(.3786+.3778+.3779); %R=25.4mm
    F1=z*1000*20.786*1.134;
elseif tip==76.2
    MASS=4.719-(.3786+.3778+.3779); %R=76.2mm
```

```
    F1=z*1000*20.786*1.074;
else
    MASS=input('Pendulum Mass = ');
    fprintf('Force Correction Factor')
    F1=input('Enter 1.00 for no scaling of force = ');
end

MBAR=0.838;
m1=MBAR+MASS; %impacting mass, kg
d=0.0554; %distance of laser break, m

% % Plot force sensor data to time t and force f from z
% plot(t*10^3,F1*10^-9)  %For output F in kN (input force data=microV),
% % t input as seconds
% xlabel('Time (ms)')
% ylabel('Force (kN)')
% hold on


%% Plot Force Data starting at t=0

i=0; n=0;
for h=1:length(t)
    i=i+1;
    F1temp=abs(F1(i)*10^-9); %-9 if chC is microV, -6 if mV
    if F1temp>.1
        n=n+1;
        F1zero(n)=F1temp;
        tsub(n)=t(i-1)*10^3;
        t1zerof(n)=t(i)*10^3-tsub(1);
    end
end
plot(t1zerof,F1zero)
xlabel('Time (ms)')
ylabel('Force (kN)')
hold on
% ---Conversion factors---
% R12.7mm tip: Force gauge: 4.5858 N = 1 mv, 1050V6 sensor
%              Dynamic correction: F_total = 1.008*F_gauge
% R25.4mm tip: Force gauge: 20.786 N = 1 mv, 1060V5 sensor
%              Dynamic correction: F_total = 1.134*F_gauge
% R50.8mm tip: Force gauge: 20.786 N = 1 mv, 1060V5 sensor
%              Dynamic correction: F_total = 1.092*F_gauge
% R76.2mm tip: Force gauge: 20.786 N = 1 mv, 1060V5 sensor
%              Dynamic correction: F_total = 1.074*F_gauge
% R101.6m tip: Force gauge: 20.786 N = 1 mv, 1060V5 sensor
%              Dynamic correction: F_total = 1.097*F_gauge
% R152.4m tip: Force gauge: 20.786 N = 1 mv, 1060V5 sensor
%              Dynamic correction: F_total = 1.098*F_gauge

F_max=max(F1)*10^-3/1000000; %peak force in kN (if FORCE(CH C) input is
microV), if in mV, remove ^-3

L=1.4224; %Length pendulum arm (m)
```

```
LB=0.70485; %length LB from pivot to centroid
fprintf('\nPeak force= %4.4f kN\n',F_max)

%%  CALCULATE IN/OUT VELOCITIES
i=0;
m=2000; %mV, not V
while m<5000
    i=i+1;
    m=l(i);
end
T1=t(i);
n=7000;
while n>5000
    i=i+1;
    n=l(i);
end
T2=t(i);
Ti=T2-T1;
v_in=d/Ti;
fprintf('vel_in= %0.4gm/s\n\n',v_in)

%% CALCULATE EFFECTIVE MASS AND KE
fprintf('Total Mass: %4.4f kg\n\n', m1)
KE=(1/6)*MBAR*LB^2*(v_in/L)^2+0.5*MASS*v_in^2;
fprintf('Kinetic Energy= %4.4f J\n',KE)
```